

Conformational plasticity of ligand-bound and ternary GPCR complexes studied by ^{19}F NMR of the β_1 -adrenergic receptor

J. Niclas Frei¹, Richard W. Broadhurst¹, Mark J. Bostock^{1,3}, Andras Solt¹, Andrew J. Y. Jones¹, Florian Gabriel¹, Aditi Tandale¹, Binesh Shrestha² and Daniel Nietlispach^{1,*}

¹Department of Biochemistry, University of Cambridge, 80 Tennis Court Road, Cambridge CB2 1GA, UK

²Protein Sciences, CBT, Novartis Institutes for BioMedical Research (NIBR), Basel, Switzerland

³Present address: Biomolecular NMR and Center for Integrated Protein Science Munich, Department Chemie, Technical University of Munich, Lichtenbergstraße 4, 85747, Garching, Germany & Institute of Structural Biology, Helmholtz Zentrum München, Ingolstädter Landstraße 1, 85764 Neuherberg, Germany.

*corresponding author: dn206@cam.ac.uk

Abstract

G-protein-coupled receptors (GPCRs) are allosteric signaling proteins that transmit an extracellular stimulus across the cell membrane. Using ^{19}F NMR and site-specific labelling, we investigate the response of the cytoplasmic region of transmembrane helices 6 and 7 of the β_1 -adrenergic receptor to agonist stimulation and coupling to a G_s -protein-mimetic nanobody. Agonist binding shows the receptor in equilibrium between two inactive states and a pre-active form, increasingly populated with higher ligand efficacy. Nanobody coupling leads to a fully active ternary receptor complex present in amounts correlating directly with agonist efficacy, consistent with partial agonism. While for different agonists the helix 6 environment in the active-state ternary complexes resides in a well-defined conformation, showing little conformational mobility, the environment of the highly conserved NPxxY motif on helix 7 remains dynamic adopting diverse, agonist-specific conformations, implying a further role of this region in receptor function. An inactive nanobody-coupled ternary receptor form is also observed.

Introduction

G-protein-coupled receptors (GPCRs) are a family of plasma membrane-embedded, seven transmembrane sensors that respond to a wide range of extracellular ligands¹. GPCRs act as signal transducers stimulating a response on the cytoplasmic side of the membrane via a range of intracellular binding partners (IBPs), including G proteins and β -arrestins^{2,3}. With just over 800 GPCRs in humans they are the largest class of membrane proteins⁴. Signal transduction occurs following ligand binding, which leads to an allosteric conformational signal response, whereupon changes induced by the binding event at the extracellular side of the receptor drive conformational rearrangements at the cytoplasmic face, leading to coupling with intracellular binding partners⁵. Due to their central role in signal transduction GPCRs are involved in a wide range of physiological processes and consequently, are key proteins in many disease pathways⁶. Class A or rhodopsin-like GPCRs are the targets for around 1/3 of currently available drugs^{6,7}.

Receptor regulation of the signaling process occurs at multiple levels, involving binding of orthosteric agonists as well as allosteric modulators such as lipids⁸. Our understanding of GPCR signaling has been greatly enhanced by crystal structures of receptors in the inactive, ligand-bound and fully-active (coupled to IBPs) states⁹⁻¹¹. In addition to this static picture, NMR spectroscopy has demonstrated that these receptors are highly dynamic proteins, which populate multiple states that are in equilibrium with each other¹². NMR has determined exchange kinetics and populations for some of these interconverting states^{13,14}. Investigations of several class A receptors have revealed that their energy landscapes are unique with the differences relating to their individual signaling properties¹⁵⁻²¹.

We investigate the conformational energy landscape of the β_1 -adrenergic receptor (β_1 AR). β -adrenergic receptors are central receptors in the sympathetic nervous system, which bind catecholamine ligands such as adrenaline or noradrenaline^{22,23}. The β_1 AR is the predominant subtype in the heart, which is targeted by drugs such as β -blockers in the context of cardiac dysfunction²².

Agonist-influenced equilibria between different receptor states of β_1 AR were recently described by ¹⁵N and ¹³C directed studies^{16,17}. In our recent ¹³C methionine NMR study, we presented evidence for equilibria between an inactive and pre-active state as well as for the existence of two interconverting ternary complexes¹⁷. Both equilibria were seen to be influenced by ligand efficacy, as evidenced by residues on transmembrane helices 5 and 6 (TM5 and TM6) located adjacent to the receptor binding pocket (M223^{5,54}, M296^{6,41}) (superscripts refer to Ballesteros-Weinstein numbering²⁴). These results corroborated and extended the identification of ligand-efficacy

dependent equilibria and allosteric signaling in β_1 AR using ^{15}N valine-probes ¹⁶.

NMR studies to date have provided detailed descriptions of β_1 AR signaling using a range of probes. However, due to a lack of suitable reporters, only a limited description of the response of the important cytoplasmic region of the receptor to activation, crucial for IBP interaction, is available. Crystal structures of receptor ternary complexes of β_1 AR show the large amplitude outward movement of TM6, typical of activated GPCRs ¹¹. Previously, both ^{15}N -labelled V280^{6,25} ¹⁶ and ^{13}C -labelled M283^{6,28} ¹⁷ located at the cytoplasmic side of TM6 were observed to be insensitive towards ligand-based receptor activation, likely due to these probes facing the detergent micelle. Furthermore, there is little information about the role of the highly conserved NPxxY structural motif on TM7 for β_1 AR during receptor activation ²⁵. After a rotamer change following agonist activation, the side chain of Y^{7.53} in the ternary complex forms a water-mediated hydrogen bond with Y^{5.58} which stabilises the fully-active state of the receptor ²⁶. The TM7-helix 8 region has also been suggested to play a substantial role in the coupling specificity of both arrestins and G proteins ^{18,27}.

We utilise the natural occurrence of C344^{7,54} positioned after the NPxxY^{7,53} motif at the end of TM7 in combination with fluorine-tagging to explore the cytoplasmic side of TM7 upon ligand binding and nanobody coupling (Fig. 1, Supplementary Fig. 1) using ^{19}F NMR. Furthermore, we introduce Cys282^{6,27} at the equivalent position to C265^{6,27} in the β_2 AR for a more detailed mechanistic investigation of the intracellular region of TM6 (Fig. 1, Supplementary Fig. 1). ^{19}F NMR studies have been widely used to investigate the conformational equilibria of GPCRs including the β_2 AR and A_{2A}AR receptors ^{18–21,28–32}. Using these two reporter cysteines combined with an NMR active ^{19}F -TET tag (Supplementary Fig. 2), we investigate the dynamic response of previously unexplored regions of the cytoplasmic face of the turkey β_1 AR to ligand binding and ternary complex formation, using a G protein-mimetic nanobody. Allosteric signal transduction from the orthosteric ligand-binding pocket on the extracellular side of β_1 AR to the cytoplasmic IBP interface, reveals a shifting equilibrium between inactive and active states, correlating with ligand efficacy. β_1 AR coupling to nanobody results in the formation of active as well as inactive ternary complexes, with the amount of active ternary complex correlating with the efficacy of the bound ligand. Hence, our study provides direct structural evidence for the formation of the active-state ternary complex in proportions reflecting the ligand efficacy, which in turn defines the subsequent level of downstream signaling β_1 AR. Interestingly, the conformational response in the two cytoplasmic regions on TM6 and TM7 of the ternary receptor complex is different. The response of TM6 indicates the formation of a single, well-ordered active-state ternary conformation in this region of the receptor, determined by the coupling partner, which is independent of the agonist type and shows little additional conformational dynamics. In contrast, TM7 in the vicinity of the NPxxY motif shows ligand-dependent conformational variability in the complex with extensive μs -to- ms dynamics and

conformational features at the cytoplasm that are determined by the bound orthosteric ligand. Beyond the stabilization of the active state, our observations suggest an involvement of the NPxxY microdomain during receptor activation in a manner that is predominantly related to the properties of the orthosteric ligand bound. This suggests a mechanistic role of this receptor region that might be independent of the coupled G protein, enabling the binding of further IBPs and resulting in a change in signaling bias or strength.

Results

Ligand binding conformational equilibria of TM6 and TM7

To obtain information on the response of the cytoplasmic region of turkey β_1 AR to ligand binding, individual samples of β_1 AR-m-TM6-Cys Δ 2 (Fig. 2a, Supplementary Note 1, Supplementary Fig. 4 & 6a) and β_1 AR-m-Cys Δ 2 (Fig. 2b, Supplementary Note 1, Supplementary Fig. 4, 5 & 6b) solubilized in LMNG detergent micelles were investigated by 1D 19 F NMR upon addition of saturating amounts of agonists, including in order of increasing efficacy for TM6 atenolol, carvedilol, alprenolol, xamoterol, isoprenaline and for TM7 atenolol, carvedilol, alprenolol, cyanopindolol, bucindolol, xamoterol, isoprenaline and the natural ligand adrenaline (Supplementary Table 1). Bucindolol and carvedilol are known to be biased agonists for β_1 AR^{33–36}. In the ligand-free apo state, A282C^{TET,6.27} on TM6 appeared as a single sharp peak, P1 (Fig. 2a). Only minor changes in chemical shift and linewidth were observed upon binding to the different agonists (Supplementary Fig. 6a, Supplementary Table 2). Although there was no systematic correlation with ligand efficacy, linewidths were slightly increased when bound to the higher efficacy agonists (Supplementary Fig. 7), suggesting some exchange broadening when bound to these latter ligands. For each of the current 19 F spectra the signal P1 could be deconvoluted with a single Lorentzian line (Supplementary Fig. 8, Supplementary Table 2). Comparing the R_2 values of apo β_1 AR and isoprenaline bound receptor substantiated the presence of a small exchange contribution to the linewidth of P1 (Supplementary Table 2). The failure to detect a more substantial response at the cytoplasmic side of TM6 parallels recent observations made in our 13 C methionine NMR study using the immediately neighboring residue on TM6, M283^{6.28}, as a probe¹⁷. Despite demonstrating via other residues e.g. M296^{6.41} located on TM6 closer to the ligand-binding pocket that β_1 AR-m responds in an efficacy dependent manner to stimulation by agonists, the detergent exposed M283^{6.28} showed only small changes¹⁷.

To examine whether P1 was undergoing sub-second conformational exchange with other very low populated states, we conducted a series of saturation transfer experiments with the apo receptor and the isoprenaline bound receptor, respectively. We scanned a region from -1100 to +1100 (+/- 2 ppm) relative to the main peak P1 in steps of 100 Hz but found no evidence of exchange.

Comparable ^{19}F NMR experiments were conducted with $\beta_1\text{AR-m-Cys}\Delta 2$ and agonists using $^{\text{TET}}\text{C344}^{7.54}$ on TM7 to probe the conformational response of the region immediately adjacent to the NPxxY $^{7.53}$ motif (Fig. 1). A single signal P2 (I_1 state) was observed for the receptor apo form that shifted gradually towards higher field as receptor samples were bound to ligands of increasing efficacy (Fig. 2b, Supplementary Fig. 6b). Although the chemical shift changes were small (< 0.06 ppm), they were accompanied by a considerable broadening of the signal linewidth on binding to agonists of higher G_s efficacy (Fig. 2c,d, Supplementary Fig. 6b). This was particularly noticeable for xamoterol, isoprenaline and adrenaline, suggesting growing contributions to the receptor linewidth due to μs -to- ms timescale exchange. Signal positions and linewidths both correlated with the efficacy of the ligand bound (Fig. 2c,d). All signals for P2 were deconvoluted with a single Lorentzian line with no evidence of multiple overlapping peaks (Supplementary Fig. 8 & 20, Supplementary Table 2). Hence, the line broadening with the receptor bound to high efficacy agonists was further investigated through ^{19}F NMR CPMG experiments that were performed at 564 and 658 MHz (^{19}F) and showed the effective removal of exchange broadening for $^{\text{TET}}\text{C344}^{7.54}$ as the pulsing rate ν_{CPMG} was increased from 100 to 5,000 Hz (Fig. 2e). No measurable exchange contribution was detected for the apo receptor. By fitting the CPMG data for xamoterol and isoprenaline and reconstructing the corresponding spectral shifts of P2 relative to the apo receptor position, exchange parameters were determined for xamoterol ($k_{\text{ex}} = 1,913 \pm 299 \text{ s}^{-1}$, $p_{I_2} = 0.11 \pm 0.01$) and isoprenaline ($k_{\text{ex}} = 2,878 \pm 317 \text{ s}^{-1}$, $p_{I_2} = 0.29 \pm 0.04$) bound receptor (Fig. 2e, Supplementary Fig. 6b, Supplementary Table 2).

Applying the saturation transfer technique to a region surrounding the P2 peak (Fig. 3) a substantial drop in the P2 intensity revealed the presence of a previously invisible receptor signal, P3 (A state), at a position 300 Hz upfield from the corresponding signal P2 (Fig. 3c). With the saturating field positioned on P3, a saturation time course was recorded for the apo receptor and for the receptor bound to isoprenaline (Fig. 3d). A reference series with the position of the saturating field held at a distance 300 Hz downfield from P2 was also acquired. Both time intensity series for P2 were fit simultaneously and analysis gave an exchange rate $k_{\text{ex}} = 6.9 \pm 1.8 \text{ s}^{-1}$ and a population $p_{P_3} = 0.20 \pm 0.04$ for the isoprenaline bound receptor. For the apo form of the receptor the population of P3 dropped further to $p_{P_3} = 0.15 \pm 0.04$, with $k_{\text{ex}} = 3.6 \pm 2.2 \text{ s}^{-1}$. All fits of the saturation data required the transverse relaxation rate R_2 of the lower populated species P3 to be set to a substantially larger value ($R_2^{P_3} = 600 \text{ Hz}$) than for the main peak P2 ($R_2^{P_2} = 80 \text{ Hz}$ for apo,

$R_2^{P2} = 140$ Hz isoprenaline bound). The broad linewidth explains why it had not been possible to observe the peak P3 directly by 1D ^{19}F NMR (Fig. 3a,b).

Formation of multiple ternary complexes with nanobody Nb6B9

To observe the ^{19}F NMR response of TM6 upon coupling to an IBP the apo receptor $\beta_1\text{AR-m-TM6-Cys}\Delta 2$ was supplemented with a two-fold excess of $\text{G}\alpha_s$ mimetic nanobody Nb6B9. This revealed the appearance of a new, lower intensity signal P4 for $\text{A282C}^{\text{TET},6.27}$ at -65.4 ppm, shifted downfield by 0.9 ppm from the P1 signal of the ligand-free apo receptor, in addition to P1 (Fig. 4a). With the same two-fold excess of nanobody, the experiment was repeated with samples of receptor bound to one of the agonists carvedilol, cyanopindolol, xamoterol or isoprenaline, respectively (Fig. 4a). Each ternary complex showed a P4 signal of very similar chemical shift, with linewidths that were narrower than those of the corresponding P1 signal (Supplementary Table 2). All of the P4 signals could be deconvoluted as a single Lorentzian line (Supplementary Fig. 8, Supplementary Table 2). A steady rise of the P4 signal intensity with increasing efficacy of the receptor-bound agonist revealed the formation of more ternary complex (A^{G^+}) with a concomitant decrease of the P1 signal intensity (Fig. 4a). The integrated relative signal area of P4 for the different nanobody complexes correlated well with the efficacy of the agonist bound ($R^2 = 0.96$) (Fig. 4c). Subsequently the same experiments were also repeated for carvedilol, xamoterol and isoprenaline with 5-fold and 10-fold excess of nanobody and revealed that for these ligands, the ternary complex formation followed saturation behavior, with the final amount of P4 determined by the agonist efficacy (Supplementary Fig. 9a).

The same series of measurements using a two-fold excess of nanobody was repeated with $\beta_1\text{AR-m-Cys}\Delta 2$ to assess the response of TM7 $^{\text{TET}}\text{C344}^{7.54}$ upon Nb6B9 binding (Fig. 4b, Supplementary Fig. 21). For each of the agonists used the experiments showed a new peak P5 for $^{\text{TET}}\text{C344}^{7.54}$ that was shifted downfield from P2 by approximately 0.7 ppm and was attributed to the active ternary receptor complex (A^{G^+}). However, in contrast to TM6, the TM7 region of the receptor in its apo form as well as when bound to the different agonists responded differently to nanobody binding, and resulted in P5 signals that varied in their position over a range of ~ 0.3 ppm, suggesting conformational differences on TM7 amongst the ternary complexes (A^{G^+}) formed (Fig. 4b, Supplementary Fig. 9c,d). In contrast to the reduction in linewidth between P1 and P4 for $\text{A282C}^{\text{TET},6.27}$ (Fig. 4a, Supplementary Table 2), the signals of P5 for $^{\text{TET}}\text{C344}^{7.54}$ were substantially broadened when compared to their corresponding P2 signal (Fig. 4b, Supplementary Table 2). Again, the relative signal area of the active ternary peaks P5 showed excellent correlation with the

efficacy of the ligands bound to the receptor (Fig. 4d), and a similar saturation behaviour as observed for TM6 upon addition of 5- and 10-fold excess of nanobody, respectively (Supplementary Fig. 9a).

Careful inspection of the signal area in the vicinity of the ligand-bound uncoupled receptor peak P2 near -65.5 ppm revealed the presence of an additional, broader peak P6 (A^{G^+}) superimposed at a position very similar to P2 (Supplementary Fig. 9b). At the larger excess of nanobody the relative size of this broad P6 signal rapidly overtook the signal intensity of the sharper P2 signal of the uncoupled receptor. The presence of P6 was easily inferred from the increasingly broader appearance of the signal at the 5- and 10-fold excess of nanobody, indicating that the signal envelope at -65.5 ppm was increasingly dominated by the presence of more P6 as the remaining free receptor (P2) eventually bound to nanobody (Supplementary Fig. 9b). Except for isoprenaline the region around P2 required two Lorentzian signals for a satisfactory deconvolution resulting in a sharper component for P2 and a broader component for P6. The broader component became increasingly more intense in the presence of larger excess in nanobody (Supplementary Fig. 8, Supplementary Table 2). With the shift positions of P2 and P6 being very similar and due to a lower signal-to-noise ratio the deconvolution of the isoprenaline receptor region around P2 returned a single Lorentzian with a linewidth between the one of the sharper P2 and the broader P6 (Supplementary Table 2). Accordingly, all studies conducted in the presence of nanobody confirmed the presence of a second, alternative Nb6B9-coupled receptor form.

Saturation transfer was used to assess a possible slow sub-second exchange between the signals P5 and P6. A saturation transfer time course with the saturation field centered on P6 of TM7 $^{TET}C344$ (384 Hz upfield from P5) in the presence of a two-fold excess in Nb6B9 showed that P5 is in slow exchange with P6, with $k_{ex} = 8.1 \pm 1.6 \text{ s}^{-1}$ (Supplementary Fig. 10a). A second pre-saturation experiment was conducted with the irradiation position further upfield from P6, at a sufficient distance (684 Hz upfield from P5) not to saturate P2 while still irradiating the broad foot of the P6 signal (Supplementary Fig. 10b). This resulted in a reduced but still noticeable response on P5 that is in agreement with the broad nature of P6 and confirmed the slow exchange process to be taking place between P5 and P6, with $k_{ex} = 8.0 \pm 1.5 \text{ s}^{-1}$ showing a similar exchange rate (Supplementary Fig. 10).

Solvent-accessibility during ternary complex formation was assessed with a soluble Gd^{3+} reagent (Supplementary Note 2).

Discussion

We investigated the cytoplasmic region of β_1 AR using ^{19}F NMR via TET fluoro-tagging of the native C344^{7,54} in TM7 and of a separately introduced A282C^{6,27} in TM6. These reporters were used to study β_1 AR in the apo form and with a range of agonists of varying efficacy (in order of increasing efficacy: atenolol, carvedilol, alprenolol, cyanopindolol, bucindolol, xamoterol, isoprenaline and the natural ligand adrenaline) as well as using a $G\alpha_s$ protein mimetic nanobody Nb6B9 to form ternary receptor complexes (Supplementary Table 1).

Our ^{19}F NMR experiments show that the ligand-free β_1 AR is mostly in an inactive state (I_1), as indicated by a single, well-defined signal, P1, for TM6 (Fig. 2a) and P2 for TM7 (Fig. 2b). This supports previous studies that focused on the transmembrane region of β_1 AR near the ligand binding pocket and showed this region of the apo receptor to be much less dynamic than when bound to full agonist^{16,17}. In view of the inherent low basal activity of the β_1 AR, the apo form is likely to be representative of an inactive state, (I_1).

Probing the receptor with a range of agonists varying in efficacy revealed that the P1 signal for A282C^{TET,6,27} showed only a relatively small response to ligand binding (Supplementary Note 3, Fig. 2a, Supplementary Fig. 6a, 12 & 13).

In contrast, while the TM7 signal P2 of ^{TET}C344^{7,54} indicated the apo receptor residing in an inactive form (I_1), the signal P2 gradually moved further upfield with increasing efficacy of the bound agonist (Fig. 2b,c, Supplementary Fig. 6b). At the same time P2 also displayed increasing line-broadening (Fig. 2d). ^{19}F CPMG relaxation dispersion experiments conducted at two fields for the receptor bound to isoprenaline revealed the presence of a fast exchange process with the receptor interconverting between two conformations, (I_1) and (I_2), with a rate $k_{\text{ex}} = 2,878 \pm 317 \text{ s}^{-1}$ (Fig. 2e). For xamoterol the exchange rate was reduced to $k_{\text{ex}} = 1,913 \pm 299 \text{ s}^{-1}$, while for the apo form of the receptor no additional exchange contribution to the linewidth was detected in the dispersion curve (Fig. 2e), in agreement with ligand-free β_1 AR mostly populating an inactive state (I_1). However, for xamoterol and isoprenaline-bound receptor the second conformation (I_2) was increasingly populated. The low population of this second state (I_2) when in the apo form ($p_{I_2} = 0.02$), with a slight increase when bound to xamoterol ($p_{I_2} = 0.11$) and isoprenaline ($p_{I_2} = 0.29$), indicates that (I_2) is likely a further inactive form of β_1 AR (Fig. 2e). The timescale of the exchange process $I_1 \rightleftharpoons I_2$ is too rapid to relate to substantial conformational rearrangements of the TM7 environment as e.g. observed crystallographically in the transition from the inactive state (PDB code 2YCY) to the fully active state adopted in the ternary complex structure (PDB code 6H7J) (Fig. 1). Therefore, this process is most likely related to a smaller change in the side chain conformation, potentially a

reorientation of the aromatic side chain of Y343^{7.53}, one of the conserved residues consistently observed to be involved in receptor activation and IBP coupling (Fig. 5)¹¹. An increase in the population of (I_2) with strong agonists such as isoprenaline suggests that this conformational change might be linked to the early stages of receptor activation, with (I_2) possibly being an on-pathway intermediate to a further downstream activated state. Agonists would therefore shift the $I_1 \rightleftharpoons I_2$ equilibrium towards (I_2), facilitating subsequent activation.

In addition to the $I_1 \rightleftharpoons I_2$ equilibrium, the existence of a further state (A) in slow exchange with the inactive (I_1, I_2) states of the receptor (signal P2) was found indirectly through saturation transfer experiments, which revealed the presence of a strongly broadened peak at position P3, not directly detectable by ¹⁹F NMR (Fig. 3). While only investigated for the apo and the isoprenaline bound receptor it became clear that the population of this state increased with ligand efficacy from $p_{P3} = 0.15$ in the apo form to $p_{P3} = 0.20$ when isoprenaline bound. Substantial broadening of this relatively low populated state prevented its direct observation by 1D ¹⁹F NMR and suggested the occurrence of substantial amounts of μ s-to-ms conformational dynamics in the vicinity of the NPxxY^{7.53} motif once the receptor was bound to full agonists. We assume that the signal P3 corresponds to a pre-active receptor state (A) that is competent to bind nanobody, subsequently upon IBP coupling leading to the fully-active state as seen in the structures of the ternary complex of the receptor (Fig. 5)³⁷. The slow rate of exchange (ISO: $k_{ex} = 6.9 \pm 1.8 \text{ s}^{-1}$, APO: $3.6 \pm 1.6 \text{ s}^{-1}$) between the states (I_1, I_2) and (A) is indicative of major structural rearrangements taking place in this region of the receptor. The exchange process ($I_1, I_2 \rightleftharpoons A$) happens on a similarly slow sub-second timescale as observed in β_2 AR for the move of TM6 away from the helix bundle when exchanging between inactive and active-like states, suggesting that cytoplasmic TM6 and TM7 rearrangements might be related and due to steric reasons occur in parallel¹⁴. Based on the reorientation of aromatic side chains in the immediate environment of C344^{7.54} we calculated an increase in shielding of 0.16 ppm due to changes in ring current shifts when moving from the inactive structure of β_1 AR (approximated by the cyanopindolol bound structure) (PDB code 2YCY) to the ternary complex with Nb80 (as an approximation of the pre-active receptor state) (PDB code 6H7J), suggesting a move of ^{TET}C344^{7.54} into a more hydrophobic environment upon reaching the pre-active state (Supplementary Fig. 14, Supplementary Table 3). This is in reasonable agreement with our experimental observation of P3 at a position 0.5 ppm upfield from the apo receptor signal P2 (Fig. 3), and suggests that the slow exchange process relates to the rotation and inward movement of the intracellular part of TM7 that allows Y^{7.53} following a change in the side chain rotamer conformation to slot behind the displaced TM6 (Fig. 1). As expected, the population of the (A) state increases with ligand efficacy, reaching 20% for isoprenaline. This is in a similar range to the 25% population found for the pre-active state using ¹³C methionine NMR, as assessed by the reporters M223^{5.54} and M296^{6.41}¹⁷. At the same time the exchange rate seems to increase with

ligand efficacy as well ($k_{\text{ex}}^{\text{ISO}} > k_{\text{ex}}^{\text{APO}}$) (Supplementary Fig. 2e).

Our observation of multiple inactive receptor states (I_1, I_2) for $\beta_1\text{AR}$ agrees with several NMR studies and MD simulations on $\beta_2\text{AR}$ ^{15,19,38–40}. The latter have suggested various intermediates between active and inactive states during deactivation simulations of $\beta_2\text{AR}$, which in some cases showed a TM7 conformation different from the inactive or active state ⁴¹. Different metastable states for $\beta_2\text{AR}$ were found, with TM6 adopting active-like outward as well as inward inactive-like conformations with TM7 not having reached its active-state like conformation.

MD simulations into the formation of a continuous internal water network during GPCR class A activation found such a network to be interrupted in the inactive state by the presence of two water-free layers of hydrophobic amino acid residues residing above the NPxxY^{7.53} motif and below the conserved Y^{7.53} that opened upon agonist activation to form a continuous water channel connecting the orthosteric binding site to the G protein interaction region ⁴². Y^{7.53} was found to transition between three rotamer conformations, representative of inactive (closed water channel), meta state (water channel closed at cytoplasm) and active state (open water channel). In the meta state, Y^{7.53} remained in a hydrophobic layer that breaks upon reaching the fully active state as a continuous water channel is formed ⁴². In agreement with a potential meta state and the postulated model of water accessibility, the environment of ^{TET}C344^{7.54} adjacent to Y^{7.53} in our postulated pre-active (A) state is more hydrophobic than in the ($I_{1,2}$) states as suggested by the upfield shift of P3 compared to P2 (Fig. 3, Supplementary Fig. 14) ⁴³. This agrees with the suggestion that in the (A) state the hydrophobic layer next to Y^{7.53} is still intact (Fig. 5). Accordingly, Y^{7.53} in the (A) state might have already partly rotated into an alternative conformation while not yet reaching the fully active state. In agreement with our experimental data this process is bound to be slow as it involves the rotation and inward shift of TM7 and depends on the outward movement of TM6 having already occurred. Therefore, we suggest that the pre-active (A) state is competent to bind nanobody but has not transitioned into the fully opened conformation yet, retaining Y^{7.53} (and accordingly ^{TET}C344^{7.54}) in a hydrophobic environment.

Nanobodies such as Nb6B9 have been used to stabilize the active state of receptors ^{44,45}. In the $\beta_2\text{AR}$ ternary complex they maintain the receptor in a conformation very similar to the one in the heterotrimeric G_s protein-bound complex ^{46,47}. Due to the smaller size of the ternary nanobody complexes and their better stability in detergents, we used Nb6B9 for our ¹⁹F NMR studies of $\beta_1\text{AR}$. Several crystal structures of $\beta_1\text{AR}$ -nanobody complexes are now available (Supplementary Fig. 15) ³⁷.

Addition of a two-fold excess of Nb6B9 to samples of β_1 AR either bound to one of the diverse partial or full agonists used or in the receptor apo form led to the formation of an active state ternary complex (A^{G+}) for each of the samples investigated, as evidenced by the appearance of a new ^{19}F NMR signal P4 for the TM6 probe (Fig. 4a) and a signal P5 for TM7 (Fig. 4b). The P4 and P5 peaks were shifted substantially downfield from the signals of the uncoupled receptors. We were unable to rationalize the observed large ^{19}F chemical shift changes between the ternary complexes and the ligand bound receptors through ring current shift calculations that relied on the known structural coordinates (Supplementary Fig. 13, Supplementary Fig. 14). It is likely, therefore, that the observed ^{19}F shift changes result mainly from variations in the solvent exposure of $A282C^{\text{TET}}$ and $^{\text{TET}}C344$ when adopting the ternary state. Although chemical shift changes for ^{19}F are difficult to predict, the effects of variations in polarity were investigated by Ye et al. where a downfield shift was found to be indicative of an increase in solvent polarity or augmented solvent exposure⁴³. Full activation into the ternary state results in the outward movement of TM6 and rotation of TM7 with the inward movement of the NPxxY^{7.53} motif (Fig. 1, Supplementary Fig. 16), that allows Y^{7.53} to adopt the conformation that is unique to the active state by forming polar contacts with Y^{5.58} on TM5 and water-mediated polar contacts to other residues, slotting behind TM6 (Fig. 1)¹¹. The large downfield shifts observed upon formation of the ternary states suggest changes in the polarity of the local environment with $A282C^{\text{TET}}$ and $^{\text{TET}}C344$ experiencing greater solvent exposure in the fully active state of the ternary complex. This can be understood as $A282C^{6.27}$ moves outwards away from the TM core, while for $C344^{7.54}$, the hydrophobic layer adjacent to the cytoplasm is now opened forming a continuous water channel between the ligand-binding pocket and cytoplasm (Fig. 5). Further discussion on the solvent exposure of the ^{19}F probe can be found in the supplementary information (Supplementary Note 4, Supplementary Fig. 11, 17 & 18).

For each agonist-bound receptor sample, the relative amount of ternary nanobody complex (A^{G+}) formed was determined by integration of the corresponding NMR signal. For both $A282C^{\text{TET}}$ (signal P4) (Fig. 4c) and $^{\text{TET}}C344$ (signal P5) (Fig. 4d), the amounts of active ternary complex (A^{G+}) in solution correlated very well with the efficacy of the bound agonist in the complex. Although ligand efficacy values are typically derived from cell-based assays, our experiments illustrate that agonist G_s directed signaling efficacy and the phenomenon of partial agonism closely relate to the total molecular amount of ternary receptor complex formed, as assessed here in vitro by two independent probes located at the cytoplasmic ends of TM6 and TM7.

For TM6, all active ternary complexes (A^{G+}) showed P4 at the same chemical shift position indicating a strong similarity in the conformational environment of $A282C^{\text{TET}}$ across the different

complexes (Fig. 4a), regardless to which ligand the receptor was bound. The signals were sharp with narrower linewidths than for the ligand-only bound receptor signals P2 (Fig. 4a, Supplementary Table 2), indicating the absence of any dynamics near A282C^{TET} that would broaden the NMR signal. This is in agreement with previous observations with full-agonist isoprenaline bound β_2 AR, which resulted in a sharper signal upon coupling to Nb80, as was assessed by a BTFMA probe attached to C265^{6,27 19}. Interestingly, our previous ¹³C NMR study on β_1 AR indicated that the region of TM6 below the binding pocket was still mobile, with the dynamics showing a dependency on the type of ligand bound, as assessed by M296^{6,41 17}. This suggests that even in the ternary state increased mobility persists in the regions of the allosteric network that are closer to the orthosteric binding pocket. In contrast, based on our ¹⁹F NMR data, TM6 seems likely to be more ordered near the cytoplasm, once the conformation that couples with the nanobody has been engaged. Accordingly, a single conformation for TM6 near A282C^{TET} is adopted (Fig. 4a). This agrees with the cytoplasmic side of TM6 in its active signaling conformation guiding the positioning of the IBP, while the type of binding partner dictates the extent of displacement of the cytoplasmic end of TM6 relative to the receptor core. Therefore, a more rigid arrangement at the cytoplasm is suggested to increase the efficiency of the signaling transfer onto the coupling partner, while the residual dynamics below the orthosteric binding pocket in the receptor core maintain the allosteric signal transmission initiated by the orthosteric ligand bound.

In contrast, the appearance of the signal P5 from the cytoplasmic region of TM7 in the same complexes varied over a wide range of 0.3 ppm with the position of P5 determined by the orthosteric ligand bound (Fig. 4b, Supplementary Fig. 9d). This indicates that ^{TET}C344^{7,54} reveals succinct ligand-dependent conformational differences in the adjacent NPxxY^{7,53} motif and/or helix 8 amongst the different agonist-bound ternary receptor complexes. Furthermore, all the ternary complex P5 signals of TM7 ^{TET}C344^{7,54} were strongly broadened, supporting the presence of substantial μ s-to-ms dynamics as this receptor region continues to sample multiple conformations (Fig. 4b, Supplementary Table 2). We tested whether the signal positions of P5 correlate with the efficacy of the ligands bound in the respective ternary complexes. A correlation would suggest that partial agonism is not only controlled via the amount of signaling complex formed but also via the adopted conformation at the cytoplasm of TM7. The weak correlation ($R^2 = 0.51$) between ligand G_s efficacy and chemical shift position of P5, however, indicated that this is not the case (Supplementary Fig. 9c). Therefore, the observed conformational variability of the NPxxY motif on TM7 seems unrelated to G_s protein signaling (Supplementary Note 5, Supplementary Fig. 15 & 19).

The difference in the conformational response of TM6 and TM7 to Nb6B9 binding is remarkable and suggests a potential role for the TM7 NPxxY^{7,53} motif that extends beyond the stabilisation of the fully active state. Possibly this might indicate a tendency for this receptor region to engage

alternative signaling pathways, be related to biased signaling, be relevant for IBP coupling specificity or reveal an additional layer of G_s independent signaling control that is determined by the orthosteric ligand. It is remarkable to note in this context that the carvedilol-bound complex resulted in the most downfield shifted peak and the largest difference to the balanced full agonist isoprenaline (Fig. 4b, Supplementary Fig. 9d). Previously, carvedilol has been associated with β_1 AR biased signaling^{33,35,36}. For the biased agonist bucindolol the effect is less pronounced with a shift similar to cyanopindolol. Accordingly, the biased agonist carvedilol might induce a conformation on TM7 of β_1 AR upon G_s protein binding that facilitates binding of further IBPs such as e.g. β -arrestin, leading to distinct cellular signaling outputs. Indeed, such complexes of GPCRs, β -arrestin and a G protein have been reported⁴⁸.

^{19}F NMR studies of the β_2 AR have previously reported a semi-independent response of the TM6 and TM7 conformational equilibria following binding of orthosteric ligands of differing bias^{18,49}. It was postulated that arrestin biased ligands preferentially activated TM7 over TM6, suggesting an involvement of TM7 in biased signaling. Our ^{19}F NMR data for the ligand-bound β_1 AR do not show such a response, possibly hindered through the inaccessibility of the P3 signal. In contrast, we observe a ligand dependent variability of the signal position for TM7 in ternary complexes of β_1 AR (Fig. 4b) that seems largely decoupled from the response of TM6. As for the β_2 AR this might indicate therefore that TM7 in β_1 AR plays a role in signal bias.

In order to assess the maximal amount of ternary complex that can be formed with nanobody we supplemented β_1 AR bound to carvedilol, xamoterol or isoprenaline, with a 2-fold, a 5-fold and a 10-fold excess of Nb6B9. Similar looking ligand-efficacy dependent saturation curves were obtained for TM6 and TM7 (Supplementary Fig. 9a). From our previous ^{13}C NMR study, it was known that at such an excess of nanobody there is no uncomplexed β_1 AR left in solution¹⁷. Hence, the P2 signal (I_1, I_2 state) of the uncoupled receptor should have vanished. Upon closer inspection of the spectrum near the position of the P2 signal of $^{\text{TET}}\text{C344}$ we realized the gradual appearance of a new, broad peak P6 located in a very similar position to P2 that grew with the amount of Nb6B9 added (Supplementary Fig. 9b). In contrast the sharper, original P2 signal of the free receptor was gradually disappearing upon nanobody addition. Deconvolution of the P2/P6 region of the spectra using two Lorentzian signals confirmed the presence of the sharper P2 signal and the broader P6 signal (Supplementary Table 2), with the intensity of the latter increasing and P2 decreasing as more nanobody was added (Supplementary Fig. 8g,h). Due to its similarly broad lineshape to the active ternary signal, P5, we conclude that in P6 the receptor is also nanobody-bound and hence also in a ternary complex. However, its signal position, similar to P2, suggests an inactive receptor complex, possibly indicating pre-coupling of the receptor to nanobody. Very likely this signal is related to the minor active ternary form (A^{G^-}) observed in our methionine ^{13}C NMR study¹⁷. This

form should also be present for TM6, however, due to the lack of dispersion in this region and the similarity in linewidths between ternary (P4 signal) and ligand-only bound receptor (P1 signal), it is not as clearly manifested except for the xamoterol complex where it can be observed through an increase of the signal linewidth at the position of P1 compared to the ligand-only bound form (Supplementary Table 2). Using saturation transfer at two offsets we established a slow sub-second timescale exchange between P5 (A^{G^+}) and P6 (A^{G^-}) (Supplementary Fig. 10).

The results of our ^{19}F NMR study are summarized in a model shown in Fig. 5. Ligand binding acts as a functional modulator by shifting the populations between interconverting inactive (I_1, I_2) and pre-active (A) states, with the latter increasingly populated with higher efficacy ligands. Conformational exchange between inactive and pre-active states takes place on a sub-second timescale, while (I_1, I_2) exchange occurs on the μs -to- ms timescale. Pre-active but also inactive receptor states can couple to Nb6B9 forming two type of ternary complexes. The latter interconvert on a slow sub-second timescale. The total amount of active complex (A^{G^+}) formed ultimately reflects the level of efficacy towards G_s signaling for a given ligand. While the TM6 environment in the active ternary state is rigid, the TM7 environment remains dynamic. The active complexes with different ligands display conformational variability in the vicinity of the NPxxY^{7.53} motif on TM7 (Fig. 5 inset), with possible functional implications. Based on concepts from MD simulations⁴², we indicate two layers consisting predominantly of hydrophobic side chains that act as hydrophobic gates (Fig. 5, dark grey areas) surrounding the NPxxY motif. These gates are disrupted in the A^{G^+} state allowing the formation of a continuous water pathway from the ligand pocket to the cytoplasm. The hydrophobicity of the environment surrounding the TM7 probe varies between the different states, as indicated by the position of the yellow sphere on the slider below each structure cartoon (Fig. 5). A^{G^-} might represent a pre-coupled form of the receptor that can convert into the active state A^{G^+} , its existence might be particular to the use of nanobody as a G_s mimetic or be related to its binding affinity, in view of the excess of nanobody over receptor used. In Fig. 5 the position of TM6 and TM7 in A^{G^-} is shown less open than in A^{G^+} , to emphasize that the receptor has not adopted the fully active state yet.

In conclusion we investigated the response of the underexplored cytoplasmic region of turkey $\beta_1\text{AR}$ to ligand activation and nanobody binding using ^{19}F NMR in combination with TET labelling of two cysteine probes located on TM6 A282C^{6.27} and TM7 C344^{7.54}. We show that allosteric signal transmission initiated by agonist binding leads to the population of different inactive and pre-active receptor states that are in equilibrium with each other, gradually shifting the receptor towards a more active state as higher efficacy ligands are used. Coupling of a G_s protein mimetic nanobody to receptors bound to agonists of varying efficacy results in the formation of an active ternary receptor complex. The total amount of the latter relates to the efficacy of the ligand bound,

indicating that signaling output is proportional to the amount of this species formed, providing a molecular link to the concept of partial agonism. The responses of TM6 and TM7 upon nanobody binding, however, are very different. The cytoplasmic side of TM6 is well ordered, determined by the IBP coupling partner, shows no evidence of μ s-to-ms dynamics and reveals the same conformation for different agonists bound. In contrast, TM7 displays distinct conformational variability in the vicinity of the NPxxY motif that depends on the agonist bound and in addition is dynamic on a μ s-to-ms timescale. These agonist-dependent conformational differences in the NPxxY motif in the ternary complexes suggest a further mechanistic role of this receptor region and indicate that the response of TM6 and TM7 are partly decoupled from each other even in the ternary states. The conformational differences at the cytoplasm of TM7 are particularly pronounced between the ternary complexes with unbiased agonists and the one with the biased agonist carvedilol, suggesting a functional role.

Methods

β_1 AR construct generation

The turkey β_1 AR-m-Cys Δ 2 construct was modified from the previously published β_1 AR-Met2- Δ 5 construct by introducing two cysteine mutations at position C85V^{2,48} and C163L^{4,47 17}. Primer sequences are given in Supplementary Table 4. Differences between the β_1 AR-m-Cys Δ 2 and the wildtype β_1 AR are truncations at the N-terminus, C-terminus and IL3, three thermostabilising mutations (R68S^{1,59}, E130W^{3,41}, F327A^{7,37}), five methionine substitution mutations (M44L^{1,35}, M48L^{1,57}, M179L^{EL2}, M281A^{IL3}, M338A^{7,48}) and four cysteine substitution mutations (C85V^{2,48}, C163L^{4,47}, C116L^{3,27} for yield improvement and C358A to remove a palmitoylation site). The five methionine mutations are not required for this work but were maintained for comparison purposes with our earlier work¹⁷. The amino acid sequence for β_1 AR-m-Cys Δ 2 is

```
MGAELLSQQWEAGLSLLLALVLLIVAGNVLVIAAIGSTQRLQTLTNLFITSLAVADLVMGLLVVPPFG
ATLVVRGTWLWGSFLCELWTSLDVLCVTASIWTLCVIAIDRYLAITSPFRYQSLMTRARAKVIILTVW
AISALVSFLPIMLHWWRDEDPQALKCYQDPGCCDFVTNRAYAIIASSIISFYIPLLIMIFVYLRVYREAK
EQIRKIDRASKRKTSRVAAMREHKALKTLGIIMGVFTLCWLPFFLVNIVNVFNRLVDPDWLFVAFNW
LGYANSAANPIIYCRSPDFRKAFKRLLAFFPRKADRRLLHHHHHHHHH.
```

The β_1 AR-m-TM6-Cys Δ 2 construct was generated from the β_1 AR-m-Cys Δ 2 construct through cysteine substitution C344S^{7,54} and introduction of the non-native cysteine C282 through mutation A282C^{6,27}. The amino acid sequence for β_1 AR-m-TM6-Cys Δ 2 is

MGAELLSQQWEAGLSLLLALVLLIVAGNVLVIAAIGSTQRLQTLTNLFITSLAVADLVMGLLVVFPF
ATLVVVRGTWLWGSFLCELWTSLDVLCVTASIWTLCVIAIDRYLAITSPFRYQSLMTRARAKVIILTVW
AISALVSFLPIMLHWWRDEDPQALKCYQDPGCCDFVTNRAYAIASSIISFYIPLLIMIFVYLRVYREAK
EQIRKIDRASKRKTSRVACMREHKALKTLGIIMGVFTLCWLPFFLVNIVNVFNRLVDPDWLFVAFNW
LGYANSAANPIIYSRSPDFRKAFKRLLAFFPRKADRRLHHHHHHHHH.

β_1 AR expression, purification and ^{19}F labelling

All receptor expressions were performed using the FlashBac baculovirus insect cell expression system. Transfection reactions for baculovirus generation were prepared by mixing 0.2 μg of pBacPak8 plasmid containing the β_1 AR expression constructs with 4 μL Cellfectin II (Thermo Fisher Scientific), 2 μL FlashBac DNA (Oxford Expression Technologies) and 100 μL of Insect Xpress medium (Lonza). The transfection reaction was incubated for 30 min at room temperature and then applied directly onto adherent SF9 insect cells seeded at a density of 0.5×10^6 cells per mL in a culture volume of 1 mL. The transfection reaction was incubated at 27 °C for 5 days shaking at 90 rpm. After incubation, the cells were visually inspected for signs of viral infection. The resulting cell supernatant containing the recombinant baculovirus was harvested (P0 virus generation) and was used for further rounds of viral amplifications.

For expression, SF9 insect cell cultures at a density of 1 to 1.5×10^6 cells per mL were infected with 4 mL virus stock per 1 L SF9 cell culture. The expression was carried out for 48 to 72 h at 27 °C shaking at 160 rpm and the cells were subsequently harvested by centrifugation (4000xg, 10 min, 4 °C). Resulting cell pellets were either used directly for β_1 AR purification or stored at -20 °C.

Extraction of the β_1 AR from insect cell membranes was performed by resuspension of the cell pellet with solubilisation buffer (20 mM Tris pH 8, 350 mM NaCl, 1% LMNG, 3 mM imidazole, Complete protease inhibitor (Roche)). The solubilisation was incubated for 1 h at 4 °C with stirring and the resulting suspension was cleared by centrifugation (175,000xg, 45 min, 4 °C). The cleared supernatant was applied onto a HisTrap FF 5 mL Nickel affinity column on an AKTA Pure (GE Healthcare) pre-washed with equilibration buffer (20 mM Tris pH 8, 350 mM NaCl, 0.02% LMNG, 3 mM imidazole). After protein binding, the column was washed in steps with the same buffer containing 3 mM, 50 mM and 250 mM imidazole, the latter eluting β_1 AR.

The labelling of the β_1 AR with the ^{19}F probe 2,2,2-Trifluoroethanethiol (TET) was performed according to Supplementary Fig. 2³². In brief, the nickel affinity chromatography elution fractions were combined and concentrated (Amicon Ultra-15 spin concentrator with 50 kDa molecular weight cutoff) to 10 μM protein concentration. To activate cysteine side chains for ^{19}F labelling, 4-4'-Dithiopyridine (commercially available as Aldrithiol-4TM, Sigma-Aldrich) was added in a tenfold molar excess (100 μM) together with oxidised glutathione in a fivefold molar excess (50 μM). The

solution was stirred at 4 °C for 20 min. After incubation, Aldrithiol-4TM and oxidised glutathione were removed by 1000x dilute concentration into 20 mM Tris pH 8, 350 mM NaCl and 0.02% LMNG. Following buffer exchange, 100 μM TET together with 50 μM oxidised glutathione were added and the solution was incubated for 30 min at 4 °C with stirring. The TET and oxidised glutathione were removed by 1000x dilute concentration into 20 mM Tris pH 8, 350 mM NaCl and 0.02% LMNG. The labelled β₁AR was further purified by alprenolol ligand affinity chromatography and the functional receptor eluted with either 1 mM atenolol or 0.1 mM alprenolol (Supplementary Fig. 21 & 22).

Although not monitored routinely as untagged receptor is invisible to our investigations the efficiency of the ¹⁹F labelling reaction was estimated from small-scale receptor preparations to be on the order of 80-95%. The estimate is based on the intensity comparison of the ¹⁹F NMR signal of free TET, released from the receptor following reduction of the S-S bond with DTT, relative to an external TET standard and the intensity of the SEC A280 signal of β₁AR prior to the labelling reaction.

Similar labelling reactions were also attempted with the reagents 3-bromo-1,1,1-trifluoroacetone (BTFA) or 2-bromo-N-(4-(trifluoromethyl)phenyl)acetamide (BTFMA), respectively (Supplementary Methods, Supplementary Fig. 3)

Expression and purification of Nb6B9

The expression and purification of Nb6B9 followed established protocols¹⁷. In brief, the nanobody Nb6B9 was expressed in BL21-RIL *E.coli* cells and the cell pellets were lysed before clearing the lysate by centrifugation (75,600xg, 4 °C, 30 min). The cleared lysate was applied onto a HisTrap FF 5 mL Nickel affinity column on an AKTA Pure (GE Healthcare) pre-washed with equilibration buffer (20 mM Tris pH 8, 150 mM NaCl) and washed with the same buffer containing 15 mM imidazole before eluting the bound protein with 250 mM imidazole. The elution fractions were further used for cation exchange chromatography using a Resource S column (GE Healthcare) pre-washed with equilibration buffer (50 mM Sodium Ascorbate, 75 mM NaCl). The nanobody was eluted from the Resource S column with a linear NaCl gradient ranging from 75 mM to 1 M NaCl. The pure Nb6B9 was finally buffer exchanged into 10 mM Tris pH 8, 150 mM NaCl and concentrated to approximately 1 mM protein concentration.

NMR experiments

NMR samples containing 5% D₂O were prepared with ligand added to a final agonist concentration

of 1 mM (atenolol, carvedilol, alprenolol, cyanopindolol, bucindolol, xamoterol, isoprenaline, adrenaline) to the apo form of β_1 AR receptor (20 - 50 μ M) solubilized in 1% LMNG. The population of the ligand-bound receptor exceeded 99.9%. Nanobody was added in two-fold molar excess for ternary complex formation, unless specified otherwise. NMR spectra were recorded at 308 K on a 600 MHz (1 H) and 700 MHz (1 H) Bruker Avance III spectrometer equipped with a 5 mm QCI HFCN/z cryoprobe (19 F 564 MHz) and a 5 mm TCI HCN/z cryoprobe (19 F 658 MHz), tuneable to 19 F (The Francis Crick Institute, London). 1D 19 F NMR data were obtained with a pulse acquire experiment recording 2,560 complex points (50 ms), using a repetition time of 1 s and 5,000 to 30,000 scans, resulting in a total experiment time varying between 2 to 12 h, ensuring that the signal-to-noise ratio was at least 30. To investigate the presence of μ s-to-ms timescale dynamics leading to line broadening of P2, 19 F CPMG relaxation dispersion measurements were recorded as a series of 1D experiments using a constant time implementation with a total transverse decay period of 10 ms, which allowed ν_{CPMG} to be increased from 100 to 5,000 Hz ($\nu_{\text{CPMG}} = 1/(4 \cdot \tau_{\text{CPMG}})$). Dispersion curves with 10 relaxation points were measured at 564 MHz (19 F) and 658 MHz (19 F) (The Francis Crick Institute), which took 2 days per series. The consistencies of the samples were monitored over the course of the relaxation dispersion series by 1D 1 H and 19 F NMR, so that signal losses due to hydrolysis of the TET-tag or receptor degradation could be corrected for.

To investigate slow exchange on the chemical shift timescale between P2 and P3, and between P5 and P6, a series of 1D saturation transfer experiments was recorded at 564 MHz (19 F) where the initial excitation pulse was preceded by a 2 s recovery delay followed by a 1,000 ms saturation period (saturation field strength of 25 Hz). For each of the experiments the position of the saturation field was incremented by 100 Hz, covering a range between -1,100 Hz and 1,100 Hz relative to the main signal of interest (P2 or P5). Comparing the pairwise intensities in the symmetrically irradiated experiments (on-resonance vs off-resonance (i.e. reference) experiment), the saturation offset with the strongest response was determined (for P3, saturation at -300 Hz relative to P2; for P6, saturation at -384 Hz relative to P5). Two time courses (8 points) were measured with the saturation length varying from 25 ms to 1,000 ms and the saturating field positioned at +/- 300 Hz (P3), or +/- 384 Hz (P6) relative to the main peak. For P6 a second time course was measured with the saturation position changed to +/- 684 Hz. Sample consistency was checked by 1D 1 H and 19 F NMR.

Solvent accessibility changes for β_1 AR-m-Cys Δ 2^{TET}C344 were assessed for the receptor in the presence of xamoterol (1 mM) and a two-fold excess in Nb6B9 through addition of increasing concentrations (0, 1, 3, 5 mM) of the Gd³⁺ paramagnetic relaxation agent gadopentetic dimeglumine (Magnevist). Signal intensities and R_2 values for P2 and P6 were analyzed as a function of Gd³⁺ concentration. R_2 values were obtained from a two-point relaxation measurement

by comparing the intensities in a CPMG experiment ($\nu_{\text{CPMG}} = 5,000$ Hz) with the CPMG reference experiment.

All acquired FIDs were apodized with 20 Hz line broadening prior to zerofilling to 64k points and FFT using Topspin 3.1. ^{19}F chemical shifts were calibrated with an internal standard of 2 μM trifluoroacetic acid (TFA) at -76.55 ppm relative to CFCl_3 . All signals P1 to P6 were deconvoluted as Lorentzian lines to obtain the R_2 values related to the linewidth at half-height (Supplementary Fig. 8, Supplementary Table 2). $R_{2,\text{eff}}$ values from CPMG data were obtained from signal intensities according to $R_{2,\text{eff}} = (1/T) \times \ln[I_1(\nu_{\text{CPMG}}) / I_0]$, with T being the length of the constant time period (10 ms), I_1 the signal intensity with the 180° pulse train and I_0 the reference intensity in the absence of the constant time period. The errors in $R_{2,\text{eff}}$ were estimated from the noise in the spectra and from spectral variation. Fitting of the CPMG relaxation dispersion data and extraction of fitting parameters was done using in-house written software based on the methodology described by Baldwin⁵⁰. The dispersion data was modeled as a two-state exchange process, with simultaneous fitting of the data recorded at two fields. Fitting was repeated for a range of offset differences $\Delta\omega$ between the exchanging states (I_1) and (I_2), ranking the results by their summed squared residuals. Combining the values from the best fit with the chemical shift changes of the P2 peak for different ligands, the exchange rate k_{ex} for $I_1 \rightleftharpoons I_2$ and the populations of the exchanging states p_{I_1} and p_{I_2} were determined. Analysis of the slow-exchange saturation transfer experiments was done based on the Bloch-McConnell formalism using in-house written software to obtain k_{ex} and p_{P3} from simultaneously fitting the on- and off-resonance time courses^{51,52}.

MD simulations

The ternary structure model of $\beta_1\text{AR}$ bound to xamoterol in complex with Nb6B9 (PDB ID 6H7N) was modified by coupling the cysteine side chain S_γ positions of C344 and A282C to TET and prepared for MD simulations with the Schrödinger 6 protein preparation wizard under the OPLS_2005 force field. The structure was embedded in a fully hydrated POPC bilayer coupled to TIP3P water molecules, using the OPLS3 force field for building the system and the steepest descent algorithm for energy minimization. MD simulation time was set to 1 ns at constant volume and temperature, followed by 1 ns at constant pressure and temperature for initial system equilibration, while further extending the simulation time to 12 ns at 300 K.

Data availability

The authors declare that relevant data supporting the findings of this study are available within the article and its Supplementary Information files or on reasonable request from the corresponding

author. The source data underlying Figs 2, 3 and 4 and Supplementary Figs 10 and 11 are provided in a Source Data file.

References

1. Rosenbaum, D. M., Rasmussen, S. G. F. & Kobilka, B. K. The structure and function of G-protein-coupled receptors. *Nature* **459**, 356–363 (2009).
2. Zhou, X. E., Melcher, K. & Xu, H. E. Understanding the GPCR biased signaling through G protein and arrestin complex structures. *Curr. Opin. Struct. Biol.* **45**, 150–159 (2017).
3. Erlandson, S. C., McMahon, C. & Kruse, A. C. Structural Basis for G Protein–Coupled Receptor Signaling. *Annu. Rev. Biophys.* **47**, 1–18 (2018).
4. Zhang, Y., Devries, M. E. & Skolnick, J. Structure modeling of all identified G protein-coupled receptors in the human genome. *PLoS Comput. Biol.* **2**, 88–99 (2006).
5. Hilger, D., Masureel, M. & Kobilka, B. K. Structure and dynamics of GPCR signaling complexes. *Nat. Struct. Mol. Biol.* **25**, 4–12 (2018).
6. Hauser, A. S., Attwood, M. M., Rask-Andersen, M., Schiöth, H. B. & Gloriam, D. E. Trends in GPCR drug discovery: new agents, targets and indications. *Nat. Rev. Drug Discov.* **16**, 829–842 (2017).
7. Sriram, K. & Insel, P. A. G Protein-Coupled Receptors as Targets for Approved Drugs: How Many Targets and How Many Drugs? *Mol. Pharmacol.* **93**, 251–258 (2018).
8. Thal, D. M., Glukhova, A., Sexton, P. M. & Christopoulos, A. Structural insights into G-protein-coupled receptor allostery. *Nature* **559**, 45–53 (2018).
9. Lebon, G., Warne, T. & Tate, C. G. Agonist-bound structures of G protein-coupled receptors. *Curr. Opin. Struct. Biol.* **22**, 482–490 (2012).
10. Thal, D. M. *et al.* Recent advances in the determination of G protein-coupled receptor structures. *Curr. Opin. Struct. Biol.* **51**, 28–34 (2018).
11. Carpenter, B. & Tate, C. G. Active state structures of G protein-coupled receptors highlight the similarities and differences in the G protein and arrestin coupling interfaces. *Curr. Opin. Struct. Biol.* **45**, 124–132 (2017).
12. Manglik, A. & Kobilka, B. The role of protein dynamics in GPCR function: Insights from the β 2AR and rhodopsin. *Curr. Opin. Cell Biol.* **27**, 136–143 (2014).
13. Bostock, M. J., Solt, A. S. & Nietlispach, D. The role of NMR spectroscopy in mapping the conformational landscape of GPCRs. *Curr. Opin. Struct. Biol.* **57**, 145–156 (2019).
14. Shimada, I., Ueda, T., Kofuku, Y., Eddy, M. T. & Wüthrich, K. GPCR drug discovery: integrating solution NMR data with crystal and cryo-EM structures. *Nat. Rev. Drug Discov.* **18**, 59–82 (2019).
15. Kofuku, Y. *et al.* Efficacy of the β 2-adrenergic receptor is determined by conformational equilibrium in the transmembrane region. *Nat. Commun.* **3**, 1–9 (2012).
16. Isogai, S. *et al.* Backbone NMR reveals allosteric signal transduction networks in the β 1-adrenergic receptor. *Nature* **530**, 237–241 (2016).
17. Solt, A. S. *et al.* Insight into partial agonism by observing multiple equilibria for ligand-bound

- and Gs-mimetic nanobody-bound β 1-Adrenergic receptor. *Nat. Commun.* **8**, 1–12 (2017).
18. Liu, J. J., Horst, R., Katritch, V., Stevens, R. C. & Wüthrich, K. Biased signaling pathways in β ₂-adrenergic receptor characterised by ¹⁹F-NMR. *Science* **335**, 1106–1110 (2012).
 19. Manglik, A. *et al.* Structural insights into the dynamic process of β ₂-adrenergic receptor signaling. *Cell* **161**, 1101–1111 (2015).
 20. Ye, L., Van Eps, N., Zimmer, M., Ernst, O. P. & Prosser, R. S. Activation of the A_{2A} adenosine G-protein-coupled receptor by conformational selection. *Nature* **533**, 265–268 (2016).
 21. Sušac, L., Eddy, M. T., Didenko, T., Stevens, R. C. & Wüthrich, K. A_{2A} adenosine receptor functional states characterized by ¹⁹F-NMR. *Proc. Natl. Acad. Sci.* **115**, 12733–12738 (2018).
 22. Taylor, M. R. G. Pharmacogenetics of the human beta-adrenergic receptors. *Pharmacogenomics J.* **7**, 29–37 (2007).
 23. Evans, B. A., Sato, M., Sarwar, M., Hutchinson, D. S. & Summers, R. J. Ligand-directed signalling at beta-adrenoceptors. *Br. J. Pharmacol.* **159**, 1022–38 (2010).
 24. Ballesteros, J. A. & Weinstein, H. Integrated methods for the construction of three-dimensional models and computational probing of structure-function relations in G protein-coupled receptors. *Methods Neurosci.* **25**, 366–428 (1995).
 25. Venkatakrisnan, A. J. *et al.* Diverse activation pathways in class A GPCRs converge near the G-protein-coupling region. *Nature* **536**, 484–487 (2016).
 26. Weis, W. I. & Kobilka, B. K. The Molecular Basis of G Protein–Coupled Receptor Activation. *Annu. Rev. Biochem.* **87**, 897–919 (2018).
 27. Wacker, D. *et al.* Structural features for functional selectivity at serotonin receptors. *Science* **340**, 615–619 (2013).
 28. Ye, L. *et al.* Mechanistic insights into allosteric regulation of the A_{2A} adenosine G protein-coupled receptor by physiological cations. *Nat. Commun.* **9**, 1372 (2018).
 29. Didenko, T., Liu, J. J., Horst, R., Stevens, R. C. & Wüthrich, K. Fluorine-19 NMR of integral membrane proteins illustrated with studies of GPCRs. *Curr. Opin. Struct. Biol.* **23**, 740–7 (2013).
 30. Kitevski-LeBlanc, J. L. & Prosser, R. S. Current applications of ¹⁹F NMR to studies of protein structure and dynamics. *Prog. Nucl. Magn. Reson. Spectrosc.* **62**, 1–33 (2012).
 31. Klein-Seetharaman, J. *et al.* Differential dynamics in the G protein-coupled receptor rhodopsin revealed by solution NMR. *Proc. Natl. Acad. Sci. U. S. A.* **101**, 3409–3413 (2004).
 32. Klein-Seetharaman, J., Getmanova, E. V., Loewen, M. C., Reeves, P. J. & Khorana, H. G. NMR spectroscopy in studies of light-induced structural changes in mammalian rhodopsin: applicability of solution (¹⁹F) NMR. *Proc. Natl. Acad. Sci. U. S. A.* **96**, 13744–13749 (1999).
 33. Wisler, J. W. *et al.* A unique mechanism of β -blocker action: Carvedilol stimulates β -arrestin

- signaling. *Proc. Natl. Acad. Sci* **104**, 16657–16662 (2007).
34. Galandrin, S. *et al.* Conformational Rearrangements and Signaling Cascades Involved in Ligand-Biased Mitogen-Activated Protein Kinase Signaling through the β 1-Adrenergic Receptor. *Mol. Pharmacol.* **74**, 162–172 (2008).
 35. Kim, I.-M. *et al.* β -Blockers alprenolol and carvedilol stimulate β -arrestin-mediated EGFR transactivation. *Proc. Natl. Acad. Sci.* **105**, 14555–14560 (2008).
 36. Warne, T., Edwards, P. C., Leslie, A. G. W. & Tate, C. G. Crystal structures of a stabilized β 1-adrenoceptor bound to the biased agonists bucindolol and carvedilol. *Structure* **20**, 841–849 (2012).
 37. Warne, T., Edwards, P. C., Doré, A. S., Leslie, A. G. W. & Tate, C. G. Molecular basis for high-affinity agonist binding in GPCRs. *Science* **364**, 775–778 (2019).
 38. Latorraca, N. R., Venkatakrishnan, A. J. & Dror, R. O. GPCR dynamics: Structures in motion. *Chem. Rev.* **117**, 139–155 (2017).
 39. Kim, T. H. *et al.* The Role of Ligands on the Equilibria Between Functional States of a G Protein-Coupled Receptor. *J. Am. Chem. Soc.* **135**, 9465–9474 (2013).
 40. Nygaard, R. *et al.* The dynamic process of β 2-adrenergic receptor activation. *Cell* **152**, 532–542 (2013).
 41. Dror, R. O. *et al.* Pathway and mechanism of drug binding to G-protein-coupled receptors. *Proc. Natl. Acad. Sci. USA* **108**, 13188–13123 (2011).
 42. Yuan, S., Filipek, S., Palczewski, K. & Vogel, H. Activation of G-protein-coupled receptors correlates with the formation of a continuous internal water pathway. *Nat. Commun.* **5**, 1–10 (2014).
 43. Ye, L., Larda, S. T., Frank Li, Y. F., Manglik, A. & Prosser, R. S. A comparison of chemical shift sensitivity of trifluoromethyl tags: optimizing resolution in ^{19}F NMR studies of proteins. *J. Biomol. NMR* **62**, 97–103 (2015).
 44. Steyaert, J. & Kobilka, B. Nanobody stabilization of G protein coupled receptor conformational states. *Curr. Opin. Struct. Biol.* **21**, 567–572 (2011).
 45. Manglik, A., Kobilka, B. K. & Steyaert, J. Nanobodies to Study G Protein–Coupled Receptor Structure and Function. *Annu. Rev. Pharmacol. Toxicol.* **57**, 19–37 (2017).
 46. Rasmussen, S. G. F. *et al.* Structure of a nanobody-stabilized active state of the β 2 adrenoceptor. *Nature* **469**, 175–180 (2011).
 47. Rasmussen, S. G. F. *et al.* Crystal structure of the β 2 adrenergic receptor–Gs protein complex. *Nature* **477**, 549–555 (2011).
 48. Thomsen, A. R. B. *et al.* GPCR-G Protein- β -Arrestin Super-Complex Mediates Sustained G Protein Signaling. *Cell* **166**, 907–919 (2016).
 49. Eddy, M. T., Didenko, T., Stevens, R. C. & Wüthrich, K. β 2-Adrenergic Receptor Conformational Response to Fusion Protein in the Third Intracellular Loop. *Structure* **24**,

2190–2197 (2016).

50. Baldwin, A. J. An exact solution for $R_{2,eff}$ in CPMG experiments in the case of two site chemical exchange. *J. Magn. Reson.* **244**, 114–124 (2014).
51. Bloch, F. Nuclear Induction. *Phys. Rev.* **70**, 460–474 (1946).
52. McConnell, H. M. Reaction Rates by Nuclear Magnetic Resonance. *J. Chem. Phys.* **28**, 430–431 (1958).

Acknowledgements

This work was funded through a Hershel Smith studentship to JNF and a BBSRC research grant to DN (BB/K01983 X/1). FG is the recipient of a DAAD scholarship. AT is grateful for financial support from the Trinity Henry Barlow Foundation, Newnham College and the Cambridge Trust. We are grateful for access to the Biomolecular NMR facility of the Department of Biochemistry (U. Cambridge) and the MRC Biomedical NMR Centre of The Francis Crick Institute (London).

Author contributions

JNF and DN designed the research. JNF made constructs, performed molecular biology, expressed and purified proteins and prepared NMR samples. AS, BS, AJYJ, FG and AT expressed and purified proteins. MJB conducted chemical shift calculations. JNF and DN collected and processed NMR data and analysed the spectra. RWB wrote in-house software for data analysis and performed relaxation data fitting. DN, JNF and MJB prepared the manuscript. DN supervised the project.

Competing interests

The authors declare no competing interests.

Figure legends

Fig. 1 Structure overlay illustrating conformational changes in β_1 AR upon activation. **a** Side-on view of β_1 AR bound to cyanopindolol, representative of the inactive state (magenta, PDB code 2YCY), and the nanobody Nb80 coupled receptor bound to isoprenaline, showing β_1 AR in the fully active state (blue, PDB code 6H7J). TM6, TM7 and helix 8 are shown in the colour of their respective state, with the G_s mimetic nanobody omitted for purposes of clarity. The ^{19}F tagged cysteines A282C^{TET, 6.27} and ^{TET}C344^{7.54} are shown with their side chains represented as sticks and the S_γ atom as coloured spheres. The structure overlay highlights the outward movement of TM6 and the rotation of TM7 upon formation of the ternary complex. **b** Enlarged view showing the NPxxY^{7.53} motif on TM7 containing the highly conserved Y343^{7.53} that upon formation of the ternary complex rotates behind TM6 and makes a water-mediated hydrogen bond with Y227^{5.58} on TM5 that stabilizes the active state. Both Y343^{7.53} and ^{TET}C344^{7.54} rotate inwards upon formation of the ternary complex. **c** Cytoplasmic view of the region shown in (b), which illustrates the clockwise rotation of Y343^{7.53} and ^{TET}C344^{7.54} on TM7.

Fig. 2 ^{19}F NMR spectroscopy of β_1 AR TM6 and TM7. The individual helices were studied by monitoring A282C^{TET} (**a**) and ^{TET}C344 (**b**), respectively, highlighting the response of the receptor to agonist binding and the formation of the ternary complex coupled to Nb6B9. All spectra were obtained at 308K, 564 MHz (^{19}F) with receptor concentrations of 20 to 30 μM and saturating ligand concentrations (1 mM). **a** ^{19}F NMR spectra are shown for A282C^{TET} for apo β_1 AR (light green), bound to full agonist isoprenaline (red) and with isoprenaline in ternary complex coupled to Nb6B9 (black). The peak corresponding to TM6 A282C^{TET} in the apo and isoprenaline bound β_1 AR (P1) appears at a chemical shift of -66.3 ppm. Addition of a two-fold molar excess of Nb6B9 causes a downfield shift of 0.8 ppm to -65.5 ppm (P4). The line marked with Δ indicates the appearance of free TET due to the slow cleavage of the S-S bond at 308 K. **b** ^{19}F NMR spectra for TM7 C344^{TET} show a peak at -65.4 ppm (P2) for the apo β_1 AR (light green). Isoprenaline binding (red) causes an upfield shift by 0.06 ppm and a doubling of the linewidth. Coupling to Nb6B9 (black) shifts the signal of the ternary complex (P5) downfield to -64.8 ppm, together with a dramatic increase in the linewidth, compared to both isoprenaline bound and apo β_1 AR. For ^{TET}C344 on TM7 the chemical shifts (**c**) and the linewidths (**d**) of P2 correlate with the G_s efficacy of the agonists tested. Chemical shifts and linewidths are shown relative to the apo receptor ($\delta = -54.42$ ppm, $\Delta\nu_{1/2} = 46$ Hz). Linear fits of the correlations are indicated by a line and R^2 values are given (ATE atenolol, CVD carvedilol, ALP alprenolol, CYA cyanopindolol, XAM xamoterol, ISO isoprenaline, ADR adrenaline). **e** Fast timescale μs -to- ms conformational dynamics of P2 assessed by ^{19}F CPMG relaxation

dispersion measurements for isoprenaline (red) (studied at ^{19}F frequencies of 564 MHz and 658 MHz) and xamoterol bound receptor (orange) (^{19}F 564 MHz). Best fit curves to the dispersion data are shown together with values for k_{ex} and ρ_{P3} (ρ_{P2}) obtained from the fits. The apo form of $\beta_1\text{AR}$ does not show any relaxation dispersion (green).

Fig. 3 ^{19}F saturation transfer experiments of $^{\text{TET}}\text{C344}$ on TM7. The experiments identify a low populated signal P3 that is in slow exchange with P2. The offset dependence of saturation for (a) the apo receptor (green), and (b) $\beta_1\text{AR}$ bound to isoprenaline (red) is probed in increments of 100 Hz. c Peak intensity ratios from pairwise experiments with saturation at symmetrical offsets reveal a maximal response at -300 Hz relative to the corresponding P2 signal (grey box). The response to saturation increases from the apo form to isoprenaline bound receptor. d Saturation time course for apo receptor (green) and $\beta_1\text{AR}$ bound to isoprenaline (red) with the irradiation field (field strength 25 Hz) in the on-resonance experiment (circles) applied at the position of P3, i.e. -300 Hz from P2. For the off-resonance reference experiment (crosses) saturation was applied at +300 Hz from P2. Best fits for the signal decays are shown by lines with values for k_{ex} and ρ_{P3} extracted from simultaneous fits indicated for isoprenaline bound receptor as well as the apo form.

Fig. 4 Ternary complex formation of $\beta_1\text{AR}$ coupled to nanobody Nb6B9. The experiments were conducted with the receptor in its apo form or in the presence of a range of agonists. All spectra were obtained at 308 K, 564 MHz (^{19}F) with receptor concentrations of 20 - 30 μM , saturating concentrations (1 mM) of agonists and a two-fold molar excess of Nb6B9 over $\beta_1\text{AR}$. ^{19}F NMR spectra of A282C $^{\text{TET}}$ (a) and $^{\text{TET}}\text{C344}$ (b) are shown for ternary complexes of $\beta_1\text{AR}$ in the apo form (light green), bound to carvedilol (brown), cyanopindolol (dark green), xamoterol (orange) and isoprenaline (red) (CVD carvedilol, CYA cyanopindolol, XAM xamoterol, ISO isoprenaline). The spectra are shown from top to bottom in increasing efficacy of the ligand bound. For reference the position of the uncoupled apo form is shown by a green dotted line (P1, P2) and the position of the ternary nanobody coupled complex with isoprenaline as a red dotted line (P4, P5). In (a) the grey dotted line (Δ) indicates the appearance of TET due to slow cleavage of the S-S bond at 308 K. The relative integrals of the ternary complexes P4 (c) and P5 (d) linearly correlate with the ligand efficacy. With increasing efficacy the amounts of P1 and P2 are decreasing. In (c) and (d) a black dashed line indicates the linear fit to the measured data points, while a grey dashed line shows the corresponding linear fit that goes through the origin (based on the assumption that no ternary complex should be formed if the ligand efficacy is 0%).

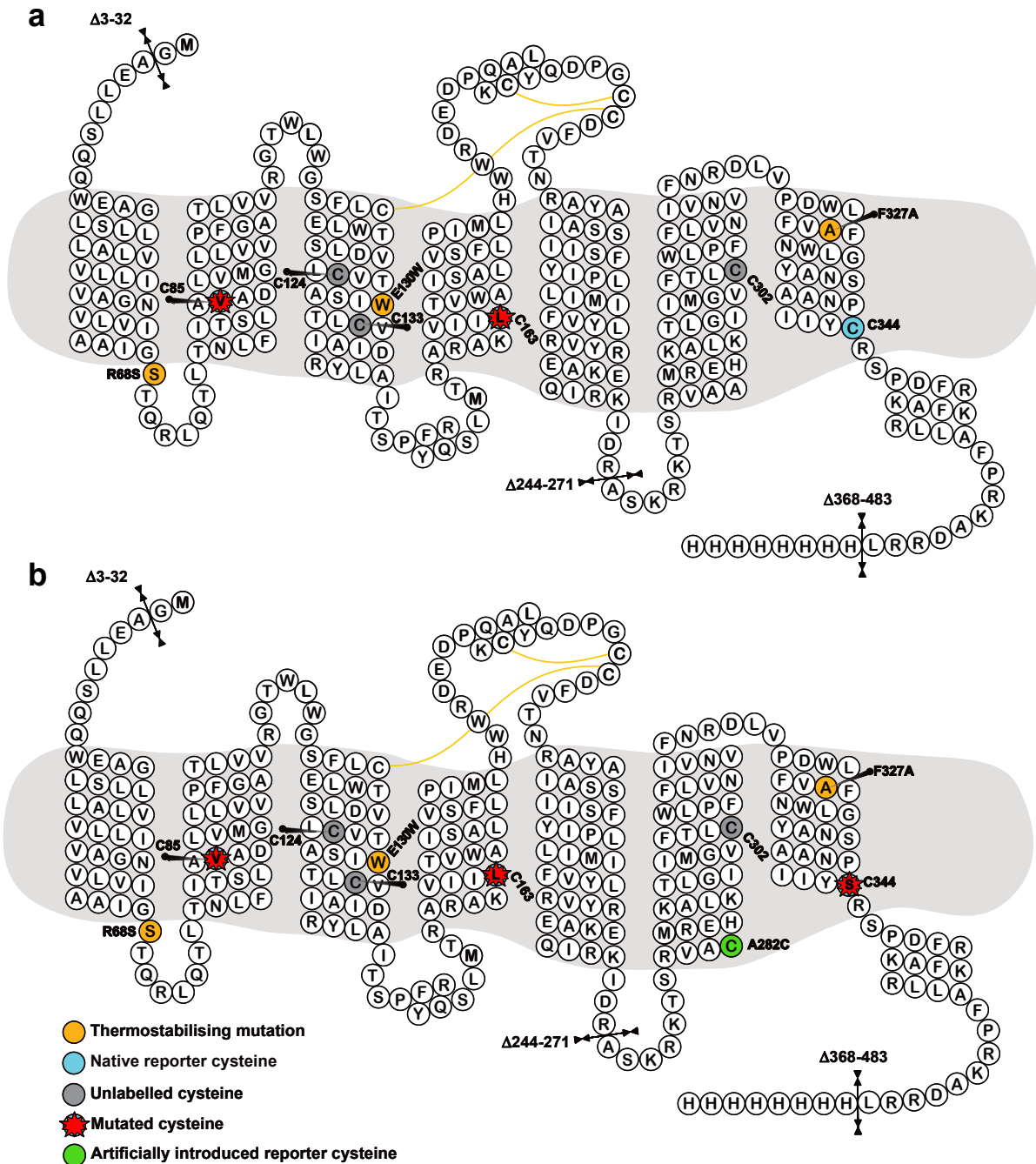
Fig. 5 Schematic overview of $\beta_1\text{AR}$ ligand activation and ternary complex formation. Cartoon cross sections spanned by TM6, TM7 and H8 with the TM7 $^{\text{TET}}\text{C344}$ ^{7.54} probes shown as yellow

spheres, adjacent to Y343^{7.53} of the NPxxY motif. The receptor exists in an equilibrium of inactive states ($I_{1,2}$) and a pre-active state (A), with the latter populated in growing amounts with increasing efficacy of the bound ligand. Nanobody Nb6B9 addition leads to the formation of a fully active ternary complex (A^{G^+}) in amounts proportional to the ligand efficacy. Nanobody binding also occurs with the inactive form of the receptor, resulting in the formation of (A^{G^-}). The latter can be considered as a pre-coupled inactive form, with inactive and active ternary complexes in slow exchange with each other. The binding interface in the (A^{G^-}) complex is shown faded, emphasizing that Nb6B9 has not yet fully engaged the epitope characteristic of the active receptor state. The (I_1) \rightleftharpoons (I_2) interchange takes place on a μ s-to-ms timescale, while the (I_2) \rightleftharpoons (A) interchange as well as the (A^{G^-}) \rightleftharpoons (A^{G^+}) exchange occurs on a slower sub-second timescale. Exchange rates, where measured, are indicated below the equilibrium arrows. In the ternary state (A^{G^+}) the cytoplasmic region of TM6 is rigid while TM7 remains dynamic on the μ s-to-ms timescale, implied by TM7 showing partly blurred. In (A^{G^+}) the conformation of TM7 in the vicinity of the NPxxY motif reveals agonist-dependent conformational differences, emphasized by TM7 showing in different colours in the enlarged region marked with (*). The grey slider below each receptor cartoon approximates the relative hydrophobic/hydrophilic extent of the TM7 ¹⁹F NMR probe surrounding in that particular state. Lipid bilayer hydrophobic regions are shown in light grey. Dark grey areas indicate transmembrane regions of the receptor with residues rich in hydrophobic side chains. These form hydrophobic gates above and below the NPxxY region (e.g. in I_1 and I_2) that shield the receptor interior against bulk water access. Blue dots on a grey background (e.g. in I_1 , I_2 and A^{G^-}) indicate ordered internal water molecules, separated from the bulk water through the hydrophobic gates (dark grey). Conformational changes upon activation disrupt the two hydrophobic side chain layers, resulting in the gradual opening of a continuous internal water pathway with cytoplasmic influx of bulk water, as indicated by the speckled grey/blue area between TM6 and TM7 in (A) and (A^{G^+}).

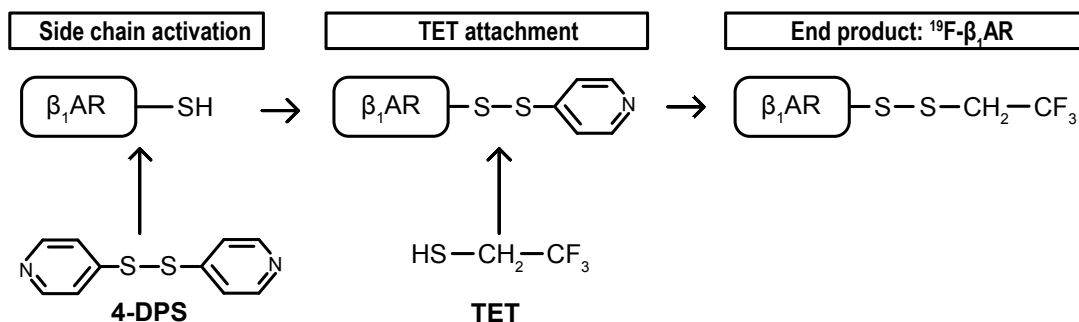
Supplementary Information

Conformational plasticity of ligand-bound and ternary GPCR complexes studied by ^{19}F NMR of the β_1 -adrenergic receptor

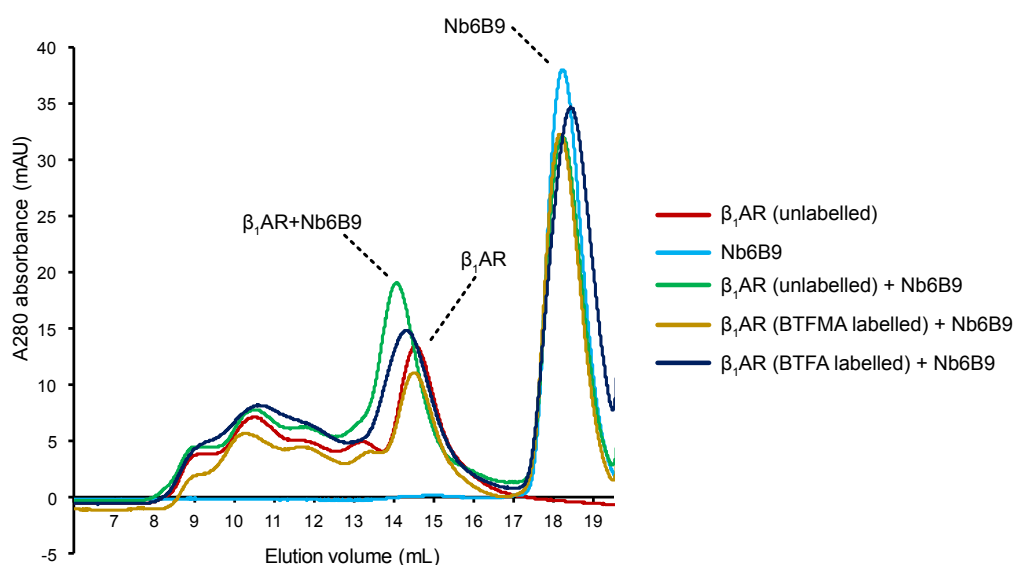
J. Niclas Frei et al.



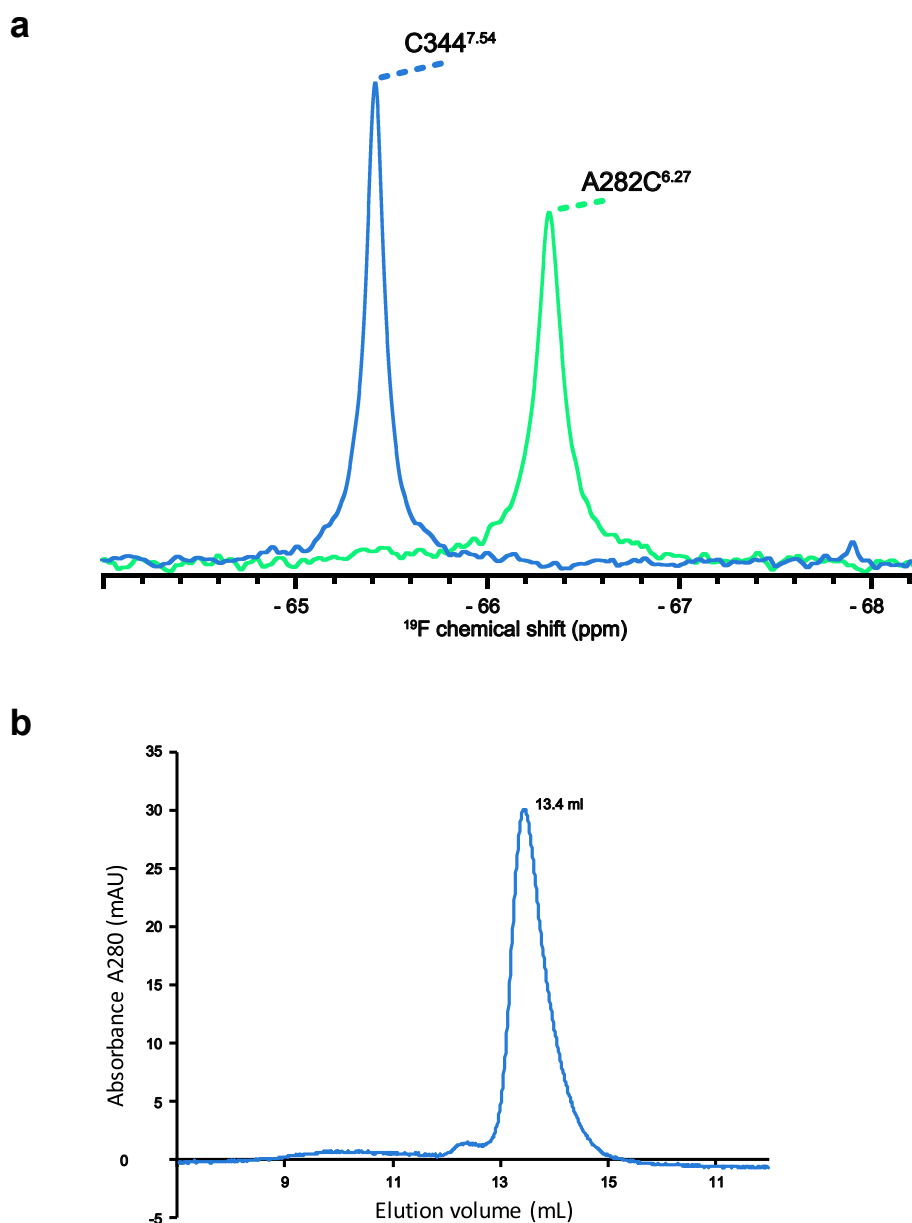
Supplementary Fig. 1 Snake diagrams of the β_1 AR constructs used for ^{19}F NMR studies. (a) The construct β_1 AR-m-Cys $\Delta 2$ used to study $^{\text{TET}}\text{C344}^{7,54}$ contains three thermostabilising mutations R68S, E130W and F327A (orange circles). The reporter C344 7,54 to be labelled with TET is shown in cyan and necessary cysteine deletion mutations C85V 2,48 and C163L 4,47 are shown as red stars. Cysteines inert to TET labelling under the given reaction conditions are shown in grey. **(b)** The construct β_1 AR-m-TM6-Cys $\Delta 2$ used to study A282C $^{\text{TET}, 6,27}$, with the residue colour coding identical to (a). In addition, the native reporter cysteine C344 7,54 was mutated to C344S while the reporter cysteine A282C (green circle) serving as TET labelling site was introduced.



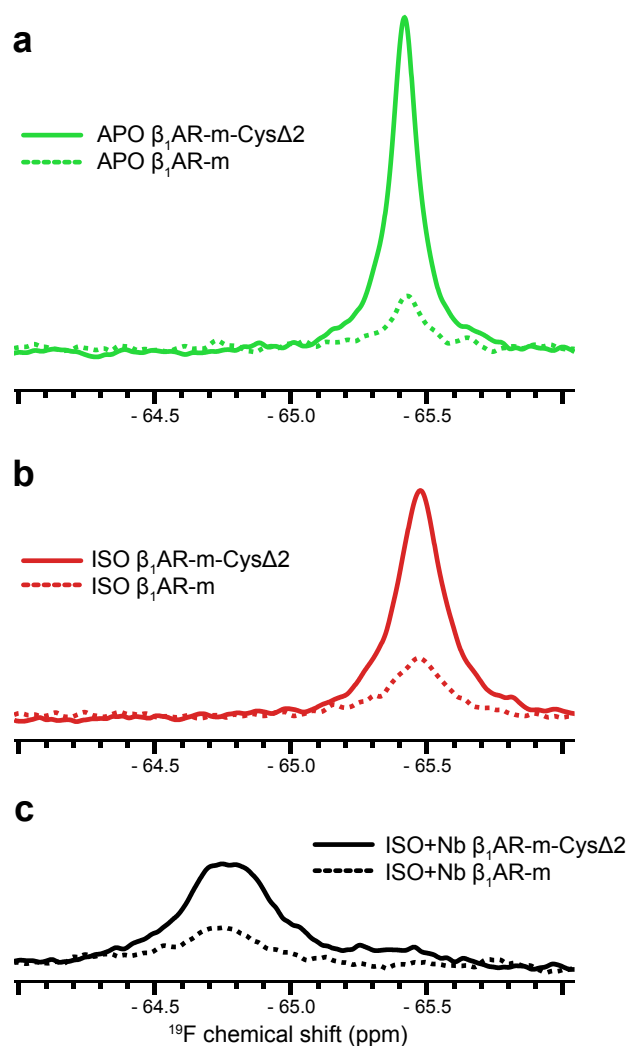
Supplementary Fig. 2 ^{19}F labelling of a cysteine sulfhydryl group of $\beta_1\text{AR}$ with TET. In a first step, accessible cysteine side chains of the $\beta_1\text{AR}$ are activated with 4,4'-Dipyridyl disulphide (4-DPS). Subsequently, the activated side chain is treated with 2,2,2'-Trifluoroethanethiol to produce the ^{19}F labelled $\beta_1\text{AR}$ ¹.



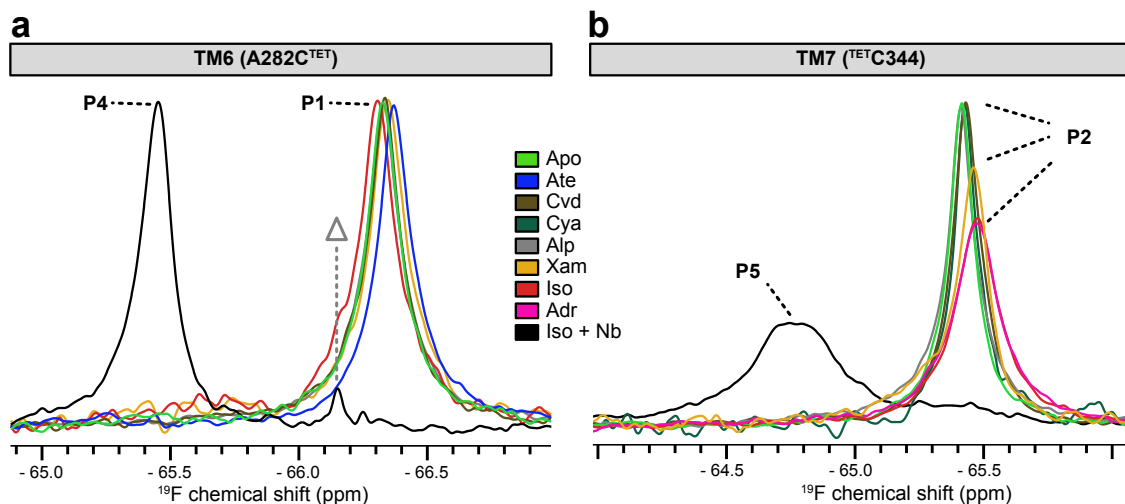
Supplementary Fig. 3 Analytical size exclusion chromatography of $\beta_1\text{AR}$ tagged with various ^{19}F reagents. Size exclusion Superdex S200 10/300 chromatography traces are shown for untagged $\beta_1\text{AR}$ (red), free Nb6B9 (cyan), untagged $\beta_1\text{AR}$ in the presence of Nb6B9 (green), $\beta_1\text{AR}$ tagged with BTFMA in the presence of Nb6B9 (orange) and $\beta_1\text{AR}$ tagged with BTFA in the presence of Nb6B9 (purple). All samples were treated with 1 mM isoprenaline prior to the addition of Nb6B9. Peak positions for the individual components are indicated by labels with dotted lines. Binding of the Nb6B9 to functional $\beta_1\text{AR}$ is indicated by a left shift in the elution volume from 14.4 mL for free receptor to 14.1 mL for the ternary complex.



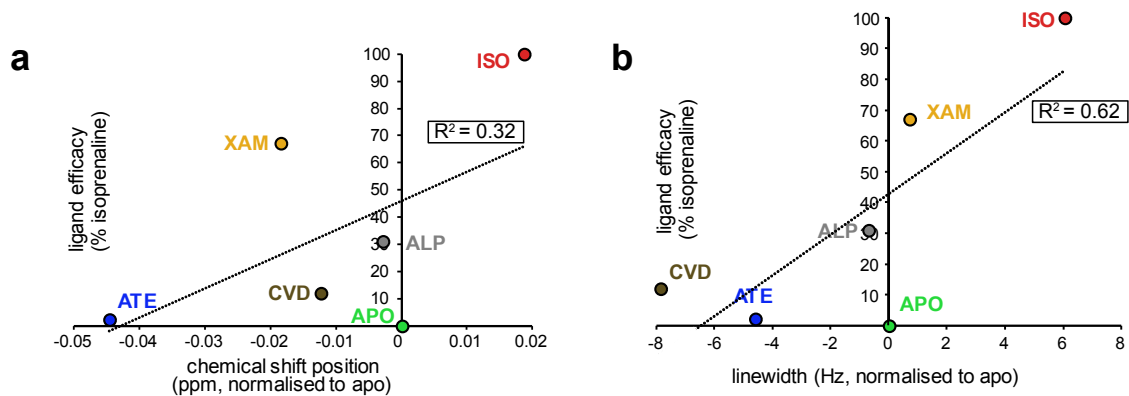
Supplementary Fig. 4 β_1 AR ^{19}F NMR samples. (a) Assignment of $^{\text{TET}}\text{C344}^{7.54}$ and $\text{A282C}^{\text{TET}, 6.27}$ signals. Individual ^{19}F NMR spectra of β_1 AR in the apo form were recorded at 564 MHz for $^{\text{TET}}\text{C344}^{7.54}$ (blue) using constructs β_1 AR-m-Cys Δ 2, and for $\text{A282C}^{\text{TET}, 6.27}$ (light green) using construct β_1 AR-m-TM6-Cys Δ 2, respectively. With the exception of the positions 344 and 282, the two constructs are identical. The observation of a single peak for $^{\text{TET}}\text{C344}^{7.54}$ and for $\text{A282C}^{\text{TET}, 6.27}$, respectively, allowed therefore the unambiguous assignment of the two labelling positions as C344 and A282C. The absence of additional background signals and the non-overlapping nature of the two NMR signals shows that no additional cysteine residues were ^{19}F labelled. All spectra were obtained at 308 K and were scaled to match their signal integrals. (b) Size exclusion Superdex S200 10/300 chromatography trace of apo β_1 AR-m-Cys Δ 2 $^{\text{TET}}\text{C344}^{7.54}$ following purification by alprenolol affinity chromatography. The high level of receptor purity and homogeneity displayed is representative of all the NMR samples used in this study.



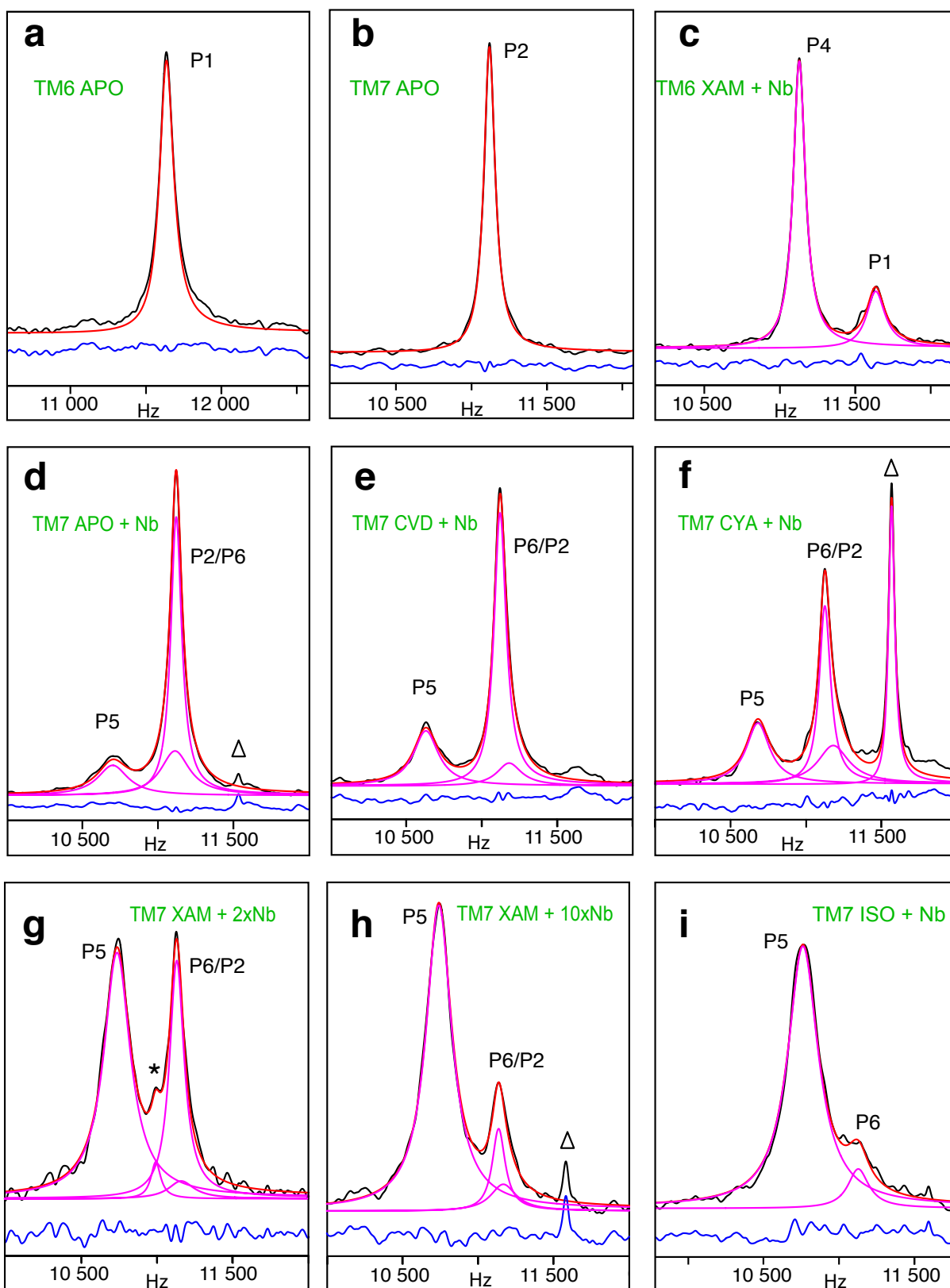
Supplementary Fig. 5 Comparison of ^{19}F NMR spectra following TET labelling of the $\beta_1\text{AR-m}$ and $\beta_1\text{AR-m-Cys}\Delta 2$ constructs. ^{19}F NMR spectra (564 MHz) were recorded under identical conditions at 308 K for the apo receptor (green) (a), receptor bound to the full agonist isoprenaline (red) (b), and in ternary complex between the $\beta_1\text{AR}$, full agonist isoprenaline and the G_s mimicking nanobody Nb6B9 (black) (c). Spectra of $\beta_1\text{AR-m-Cys}\Delta 2$ are shown as solid lines and of $\beta_1\text{AR-m}$ as dashed lines, respectively. Corresponding spectra of both constructs are virtually identical, except for the lower intensity for $\beta_1\text{AR-m}$, which is evidence for the reduced yield in protein uniquely labelled at $^{\text{TET}}\text{C344}^{7.54}$ when using this construct. Labelling of $\beta_1\text{AR-m}$ at multiple Cys sites that compete with C344 lead to insoluble protein that was easily separated from the wanted $^{\text{TET}}\text{C344}^{7.54}$ product, but resulted in dramatically reduced yields, which in view of their identical spectroscopic behaviour justified the use of the $\beta_1\text{AR-m-Cys}\Delta 2$ for ^{19}F NMR spectroscopy.



Supplementary Fig. 6 ¹⁹F NMR spectra of TM6 TET^{C344}^{7.54} and TM7 A282C^{TET, 6.27} for ligand bound states of β_1 AR investigated in this study. ¹⁹F NMR spectra (564 MHz) are shown as overlays for all ligands and the ternary complex with full agonist isoprenaline and nanobody Nb6B9 for TM6 A282C^{TET, 6.27} (a) and TM7 TET^{C344}^{7.54} (b). The colours for the individual ligands bound are indicated in the legend on the figure. All spectra were obtained at 308 K and are shown scaled according to their signal integrals. The positions for peaks P1, P2, P4 and P5 representing functional states of β_1 AR as discussed in the main text are indicated. The signal marked with Δ relates to the release of TET due to slow cleavage of the S-S bond at 308 K. Values for the chemical shift positions and linewidths of the signals can be found in Supplementary Table 2.

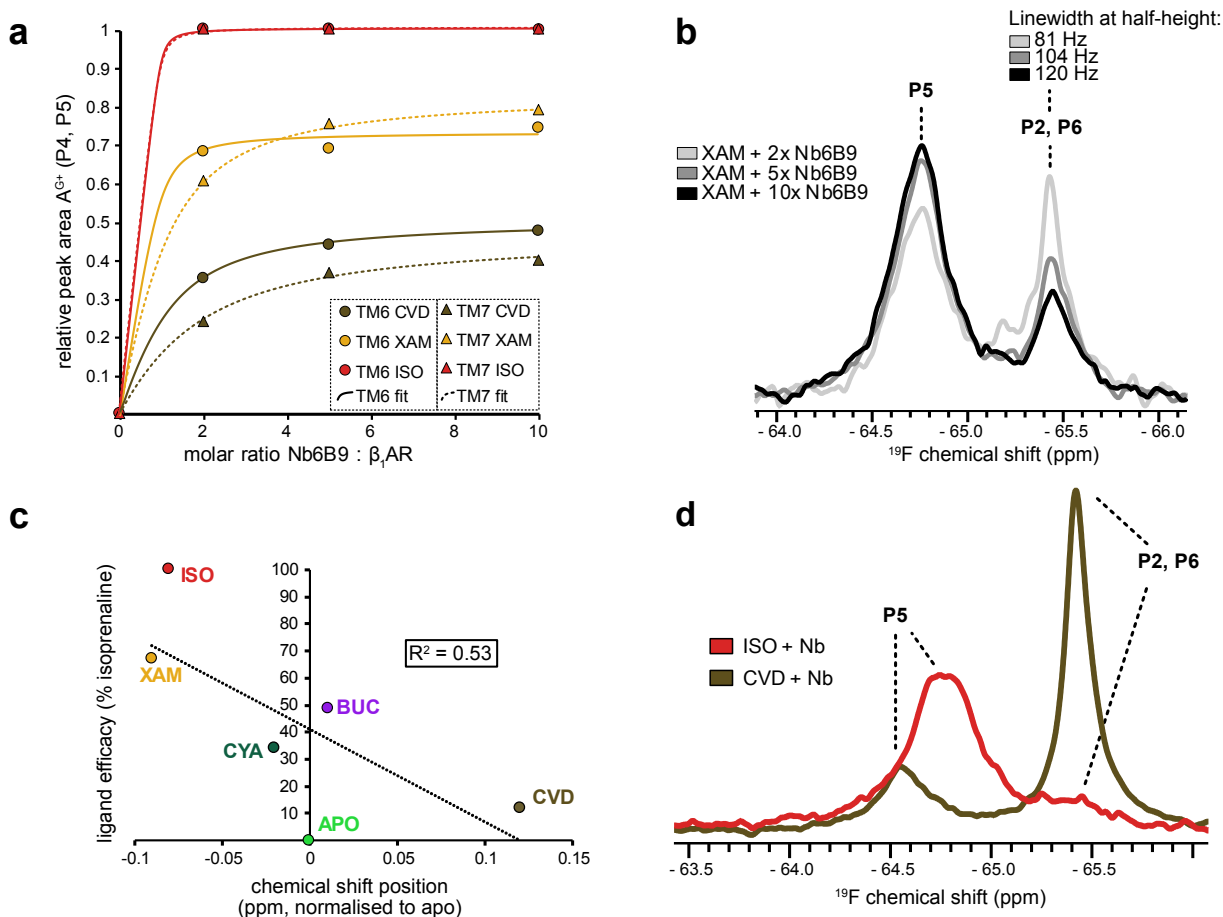


Supplementary Fig. 7 TM6 A282C^{TET,6.27} does not show any significant linear correlation between the P1 ¹⁹F NMR chemical shift and ligand efficacy, or between the P1 linewidth and ligand efficacy. (a) The correlation between the chemical shift position of P1 and the efficacy of ligands towards G_s signalling shows a very weak correlation. The following conditions were assessed: apo receptor (green), atenolol (blue), carvedilol (brown), alprenolol (grey), xamoterol (orange) and isoprenaline (red). All shift positions were normalised to the chemical shift of P1 for the apo receptor at -66.33 ppm. G_s efficacies were normalised to the isoprenaline G_s efficacy which was set to 100%. A dotted line shows the best linear fit of the data points and an R² value of 0.32 indicates a relatively poor fit. **(b)** Similarly, the correlation of the linewidth of P1 with the G_s efficacy is shown using the same receptor states as in (a). Linewidths were measured as widths of P1 at the peak half-height. All linewidths were normalised relative to the linewidth of P1 for the apo receptor (73 Hz). G_s efficacies are normalised to the isoprenaline G_s efficacy which was set to 100%. The relatively poor quality of the linear fit is indicated by an R² value of 0.62.



Supplementary Fig. 8 1D ^{19}F spectrum deconvolutions. Overlay of 1D ^{19}F NMR spectra (experimental data) (black), the spectral deconvolutions as Lorentzian signals (purple), the simulated 1D spectra consisting of the sum of the individual deconvoluted signals (red), and the residual error of the deconvolutions (blue). Each spectrum corresponds to a region of 2,000 Hz centered on the observable peaks. The peak labelled Δ corresponds to free TET that is released

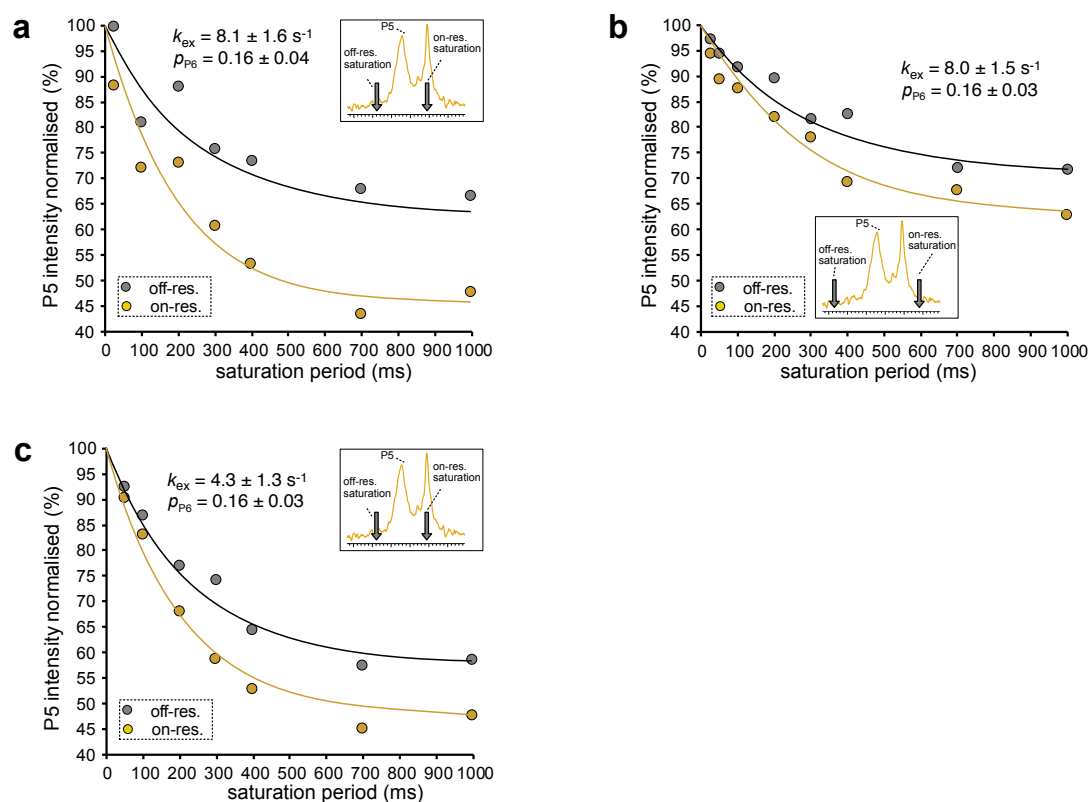
over time due to slow cleavage of the S-S bond at 308 K. The signal labelled with * is a degradation product of unknown composition ($R_2 = 60$ Hz). β_1 AR TM6, A282C^{TET, 6.27}: **(a)** apo form, **(c)** apo receptor in the presence of Nb6B9. β_1 AR TM7, ^{TET}C344^{7.54}: **(b)** apo form, **(d)** apo receptor in the presence of Nb6B9, **(e-i)** agonist bound receptor in the presence of Nb6B9, with carvedilol **(e)**, cyanopindolol **(f)**, xamoterol **(g,h)**, and isoprenaline **(i)**. Excess ratio of nanobody over receptor was two-fold except for (h) where the excess was ten-fold. All the apo and ligand bound receptor spectra for TM6 (A282C^{TET, 6.27}) and TM7 (^{TET}C344^{7.54}) (see Supplementary Table 2) were deconvoluted with a single Lorentzian line for P1 (a) and for P2 (b), respectively. The downfield signal for the spectra in the presence of nanobody was deconvoluted as a single line both for TM6 P4 (c) and for TM7 P5 (d-i), respectively. The upfield signal was deconvoluted as a single signal for TM6 P1 (c) (see Supplementary Table 2), two signals for the P2/P6 region of TM7 (d-h), and as a single signal for the P2/P6 region of the isoprenaline bound ternary receptor TM7 (i).



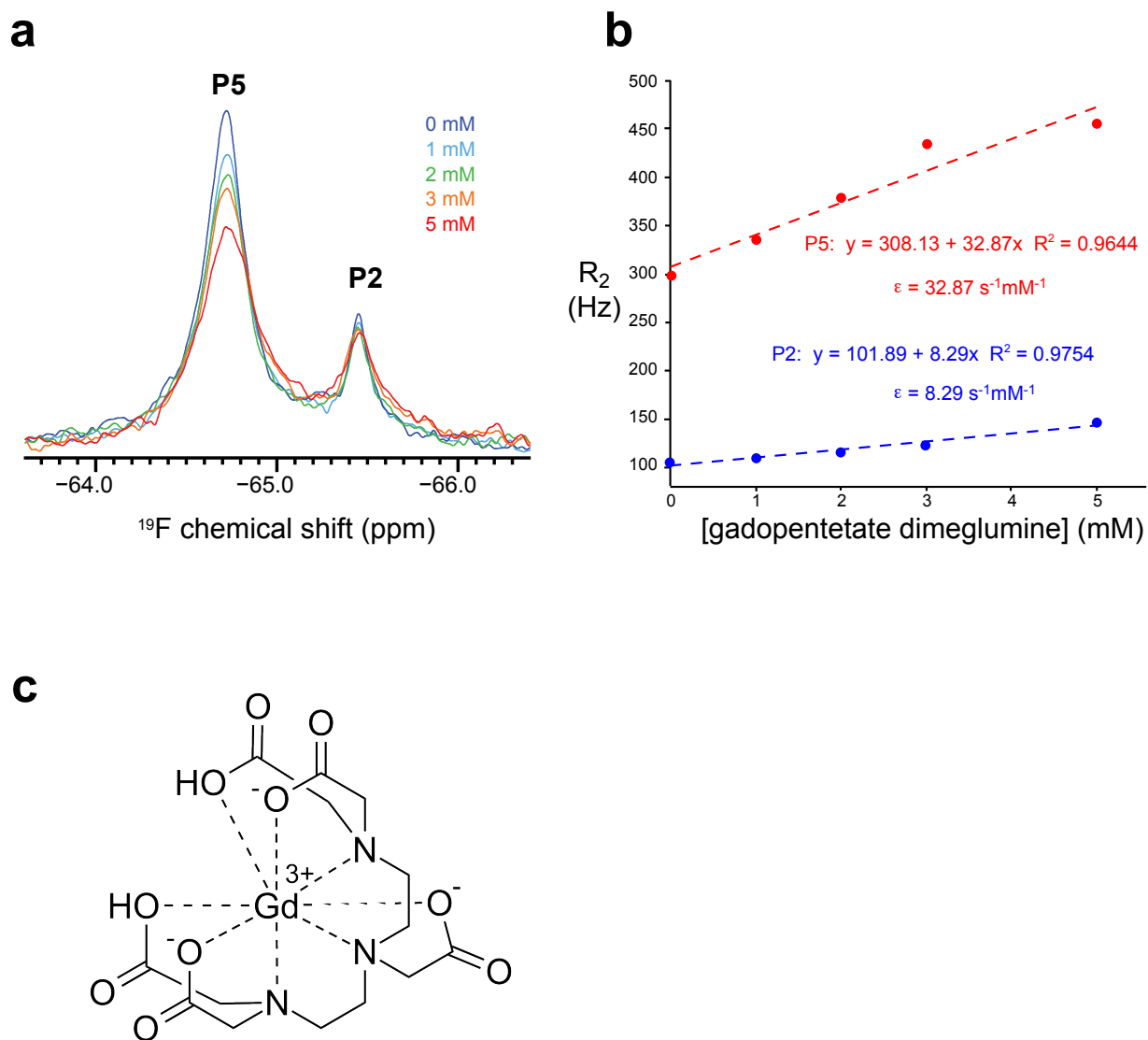
Supplementary Fig. 9 ^{19}F NMR analysis of ternary complex formation.

(a) Nanobody Nb6B9 was titrated to the receptor in molar nanobody excesses of twofold, fivefold and tenfold with the receptor individually labelled at positions $^{\text{TET}}\text{C344}^{7.54}$ or $\text{A282C}^{\text{TET}, 6.27}$. The amount of active ternary receptor (A^{G^+}) formed was monitored as the peak integral of P4 for $\text{A282C}^{\text{TET}, 6.27}$ or P5 for $^{\text{TET}}\text{C344}^{7.54}$, respectively. The amounts of P4 and P5 reach a plateau as the amount of nanobody is increased. Circles indicate the relative peak area of P4 for $\text{A282C}^{\text{TET}, 6.27}$ and triangles show the relative peak area of P5 for $^{\text{TET}}\text{C344}^{7.54}$. Data was collected for ternary complexes with ligands carvedilol (brown), xamoterol (orange) and isoprenaline (red). **(b)** Overlay of individual 1D ^{19}F NMR spectra of the nanobody titration leading to the formation of the ternary complex P5 (A^{G^+}) in increasing amounts as measured by $^{\text{TET}}\text{C344}^{7.54}$, using a twofold (light grey), fivefold (dark grey) and tenfold (black) nanobody molar excess. The positions of P5 (A^{G^+}) and the overlapped region consisting of P2 ($I_{1,2}$) and P6 (A^{G^-}) are indicated by dotted lines. With increasing excess of nanobody, the linewidth of the broader peak P6 increasingly dominates the overall linewidth of the overlapped P2/P6 region. The latter agrees with an increase in the amount of the broader P6 (A^{G^-}) with the amount of the sharper P2 ($I_{1,2}$) decreasing as nanobody is added in larger excess. The linewidths of this overlapped P2/P6 region are given above the peak annotation. **(c)** Correlating the chemical shift positions of the P5 signal of $^{\text{TET}}\text{C344}^{7.54}$ for the active nanobody-

bound complexes (A^{G+}) with the ligand efficacy reveals a poor linear fit ($R^2 = 0.51$). Complexes (A^{G+}) were formed for the apo receptor (light green) and with β_1 AR bound to the ligands carvedilol (brown), cyanopindolol (dark green), bucindolol (purple), xamoterol (orange) and isoprenaline (red), respectively. **(d)** Differences in the chemical shift positions of the P5 signal for ternary complexes (A^{G+}) with the receptor bound to different agonists are revealed. The ^{19}F NMR spectra of $^{\text{TET}}\text{C344}^{7,54}$ for the ternary complexes with ligands isoprenaline (red) and carvedilol (brown) were recorded in the presence of a twofold molar excess of nanobody. The positions of the peaks are indicated by dotted lines. Individual chemical shift and linewidth informations are given in Supplementary Table 2.

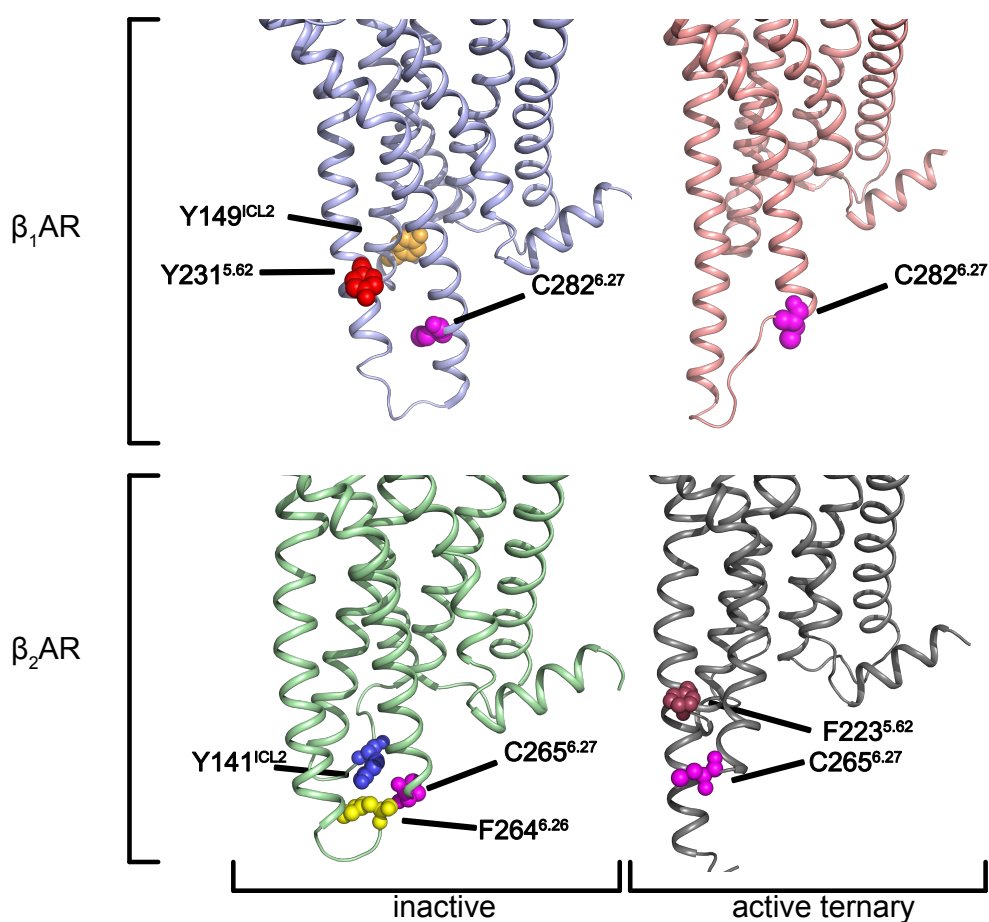


Supplementary Fig. 10 ^{19}F NMR saturation transfer time courses for $\beta_1\text{AR}$ in ternary complex with xamoterol and Nb6B9. The plots show normalised signal intensities for P5 following on- and off-resonance saturation. The insets show the positions of the saturation field (grey arrows) relative to the observed peak P5 (A^{G^+}). **(a)** The saturation field (field strength 25 Hz) was positioned 384 Hz upfield from P5 (A^{G^+}) and the intensities of the P5 signal measured for saturation times ranging from 25 ms to 1000 ms (yellow dots). A second off-resonance reference experiment was conducted with the saturation field positioned 384 Hz downfield from P5 (grey dots). The on-resonance position corresponds to the location of the broad peak P6 (A^{G^-}). **(b)** Similar saturation transfer time course with the saturation field positioned 684 Hz upfield (yellow dots) and downfield (grey dots) from P5, to selectively saturate the broad foot of the upfield P6 peak, while minimizing saturation of P2. The exchange rates k_{ex} from (a) and (b) obtained from simultaneously fitting on-resonance and off-resonance (reference) experiments are very similar, suggesting that the exchange is taking place between P5 and P6, without any involvement of P2. **(c)** Similar time course to (a) but using a ten-fold excess in Nb6B9, while a two-fold excess was used for (a) and (b). The data shows the normalised intensities of P5 after saturation at the respective positions shown in the insets displaying the spectra. Compared to the saturation in (a) the response in (b) is reduced.

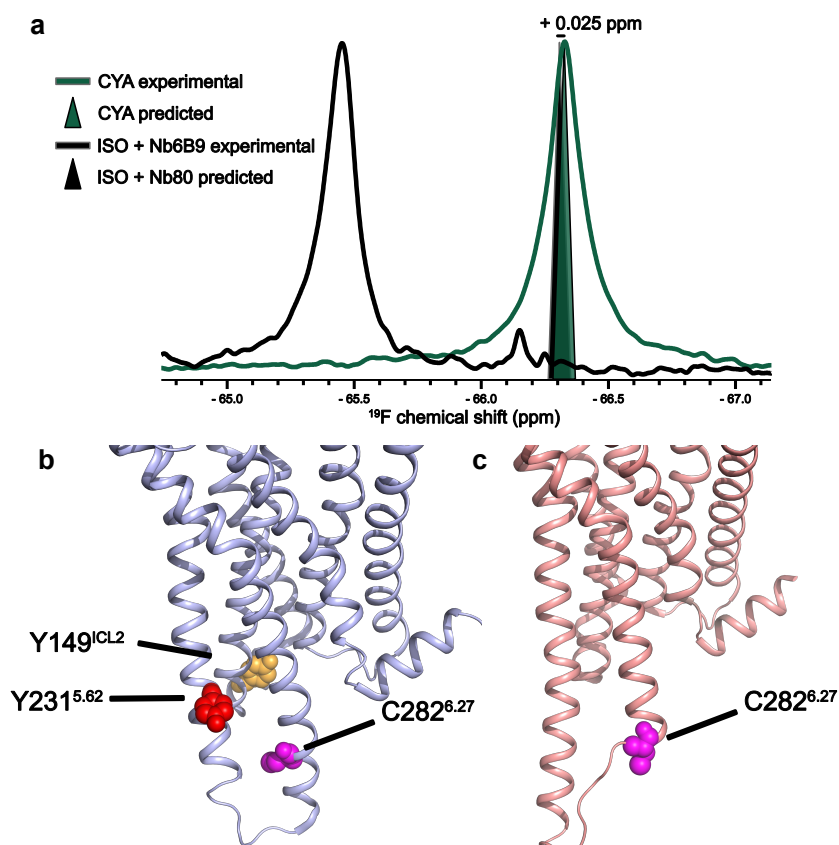


Supplementary Fig. 11 Probing the solvent-accessibility of TM7^{TET}C344^{7.54} through the addition of the Gd³⁺ paramagnetic relaxation reagent gadopentetate dimeglumine (Magnevist).

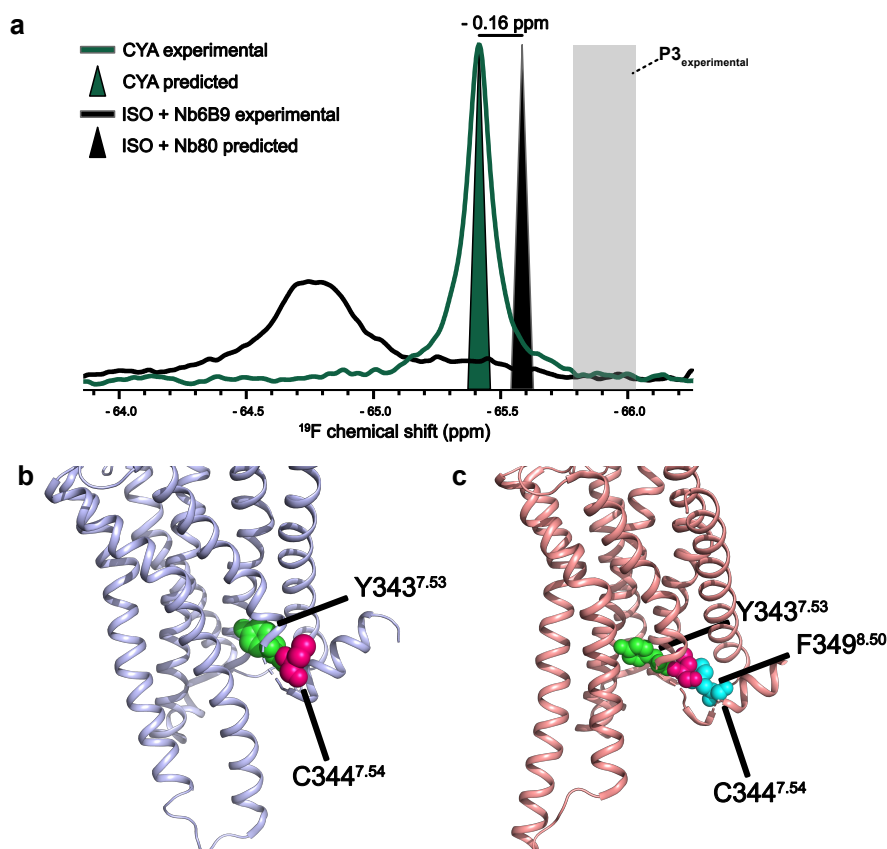
(a) Intensities of the P5 signal of the ternary xamoterol-bound receptor coupled to nanobody Nb6N9 and the P2 signal of xamoterol-bound β_1 AR following addition of increasing amounts of Magnevist (0 mM (blue), 1 mM (light blue), 2 mM (green), 3 mM (orange), 5 mM (red)). Under the chosen starting conditions (1 mM xamoterol, two-fold Nb6B9 excess) the initial ratio (0 mM Gd³⁺) of P5 to P2 was 60:40, allowing a side-by-side assessment of the effect of Gd³⁺ addition on P2 and P5. **(b)** R_2 rates for P5 (red) and P2 (blue) determined from a two-point relaxation measurement (Intensity in a CPMG experiment with $\nu_{\text{CPMG}} = 5,000$ Hz and a constant time of 2.5 ms versus a CPMG reference plane without the 2.5 ms delay). The relaxation enhancements ϵ due to the addition of the relaxation reagent are given by the slopes of the linear fits, as $32.87 \text{ s}^{-1}\text{mM}^{-1}$ for the ternary complex and $8.29 \text{ s}^{-1}\text{mM}^{-1}$ for the ligand-bound state. **(c)** Molecular structure of gadopentetate dimeglumine (Magnevist).



Supplementary Fig. 12 Comparing the location of aromatic residues in the vicinity of the TM6 reporter for β_1 AR and β_2 AR. The top panel shows the comparison of inactive (blue, PDB code 2YCY) and active (pink, PDB code 6H7J) crystal structures of the β_1 AR. The position of aromatic residues influencing the chemical shift of C282^{6.27} (magenta) are shown in both structures as spheres. For the inactive β_1 AR, Y149^{ICL2} and Y231^{5.62} are shown in orange and red, respectively. Due to their extended distance to C282^{6.27} they only minimally contribute to chemical shift changes. For the active β_1 AR structure, there are no aromatic residues in the vicinity of C282^{6.27}. Between inactive and active β_1 AR, therefore, the predicted changes in the aromatic environment of C282^{6.27} are small, resulting in negligible chemical shift differences between both. This fits well with the experimental results. The bottom panel shows the same situation for inactive (green, PDB code 4GBR) and active (grey, PDB code 3SN6) β_2 AR. Aromatic residues that have an effect on C265^{6.27} (magenta) are Y141^{ICL2} and F264^{6.26} in blue and yellow, respectively. Their close distance to C265^{6.27} make them more likely to contribute towards chemical shift changes than for the corresponding position in the β_1 AR, while the chemical shift of C265^{6.27} of β_2 AR in the active state is influenced by the nearby F223^{5.62} (purple). Between inactive and active β_2 AR the changes in the aromatic environment of C265^{6.27} are extensive therefore, resulting in substantial chemical shift changes due to variations in aromatic ring current shifts. Again, this is in agreement with the experimental data ².

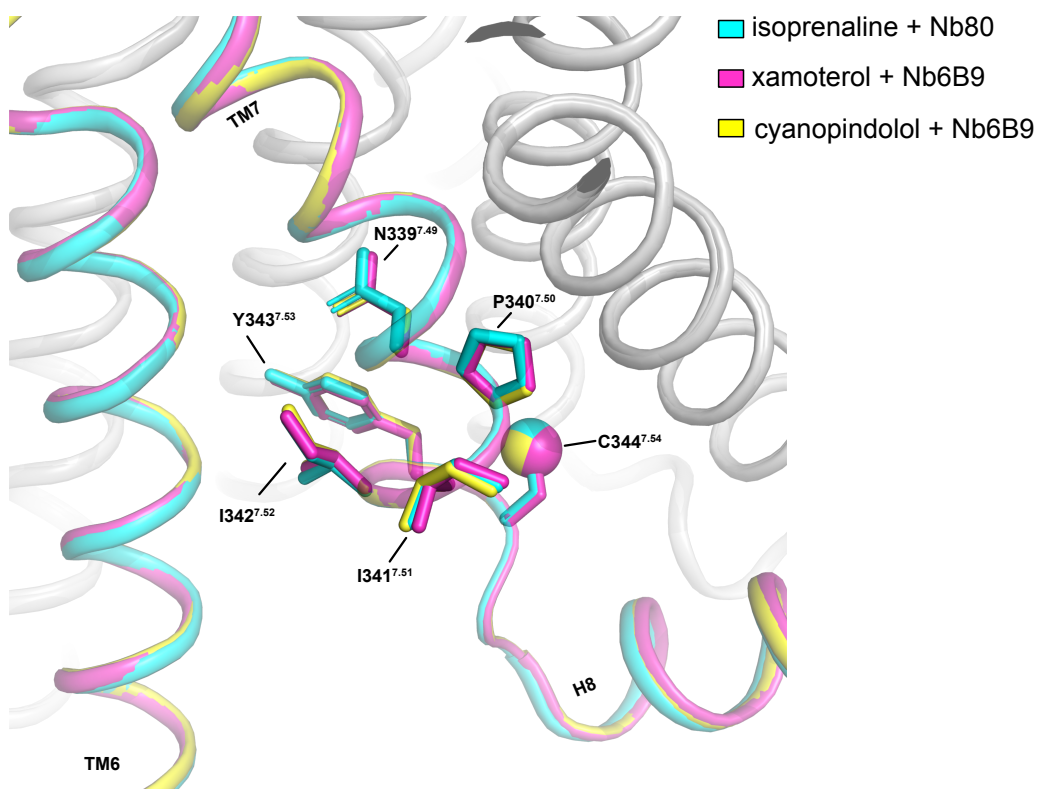


Supplementary Fig. 13 Comparison of experimentally observed and calculated chemical shifts for TM6 A282C^{TET, 6.27}. (a) Experimental ¹⁹F NMR spectra are shown as solid lines for the cyanopindolol bound β_1 AR (green) representing the inactive receptor and β_1 AR in complex with full agonist isoprenaline and nanobody Nb6B9 (black) representing the signaling active receptor. Chemical shift predictions were performed using the molecular analysis software MOLMOL³ (see Supplementary Table 3). Position of predicted chemical shifts are shown as large triangles for the cyanopindolol bound β_1 AR (green) and full agonist isoprenaline and nanobody Nb80 bound β_1 AR (black). The predicted position of the cyanopindolol bound receptor was normalized to the experimentally observed peak position of the cyanopindolol bound receptor. The distance between the predicted chemical shift positions of both receptor states is 0.025 ppm and is indicated as a black line. (b) The crystal structure of the cyanopindolol bound β_1 AR (PDB code 2YCY) is shown as a blue cartoon. The position of A282C^{TET, 6.27} is shown as magenta spheres. The only relatively close aromatic residues to A282C^{TET, 6.27} are Y149^{ICL2} shown in orange and Y231^{5.62} depicted in red. Both residues, however, are too distant to A282C^{TET} to considerably influence its chemical shift. (c) The crystal structure of the isoprenaline and nanobody Nb80 bound β_1 AR (PDB code 6H7J) is shown as a pink cartoon. The position of A282C^{TET, 6.27} is shown as magenta spheres. Based on the crystal structure coordinates MOLMOL³ predicts no aromatic residues in the vicinity of A282C^{TET, 6.27} that would contribute to a chemical shift change. Not surprisingly therefore inactive and pre-active states have very comparable chemical shifts.

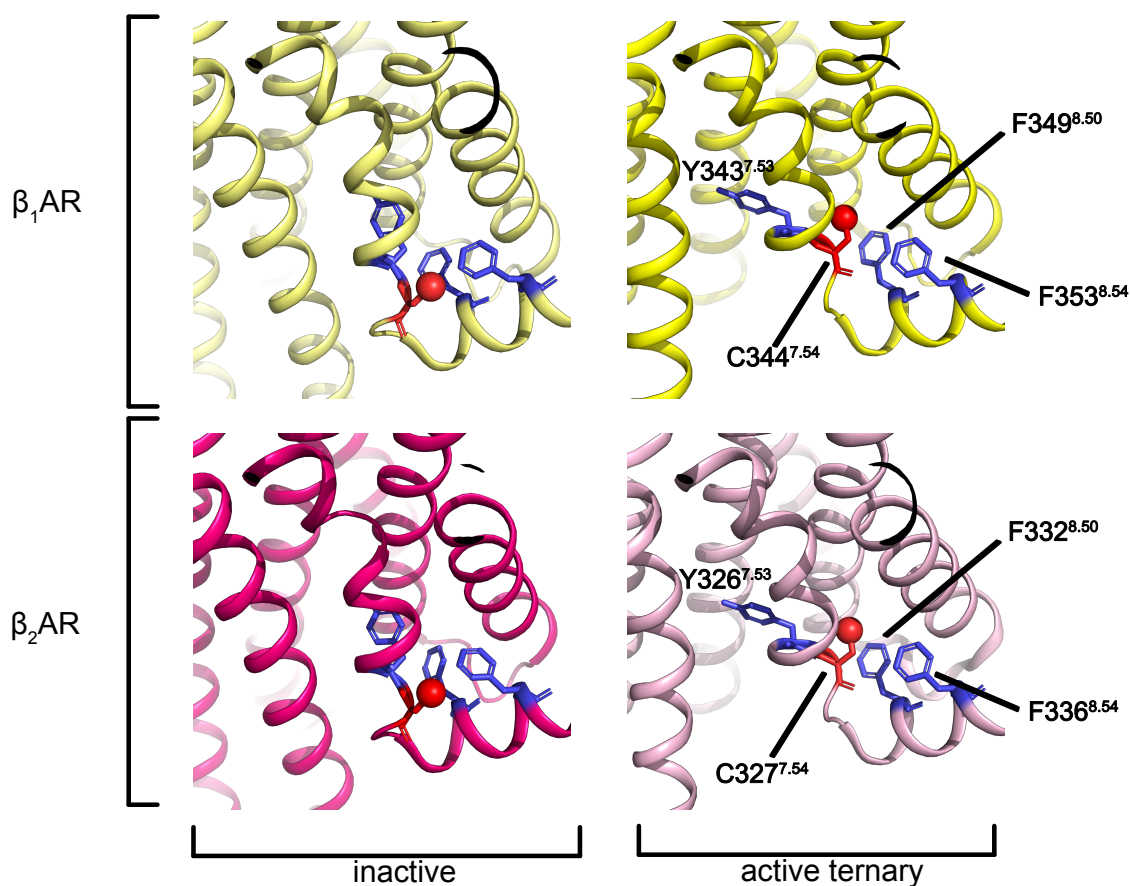


Supplementary Fig. 14 Comparison of experimentally observed and calculated chemical shift values for TM7^{TET}C344^{7.54}. (a) Experimental ¹⁹F NMR spectra are shown as solid lines for the cyanopindolol bound β_1 AR (green) for the receptor in a close to inactive conformation, and β_1 AR in ternary complex with full agonist isoprenaline and nanobody Nb6B9 (black) for the signaling active receptor state. Predicted ¹⁹F chemical shift changes were obtained in MOLMOL³ using the Johnson-Bovey equation⁴, considering solely contributions from aromatic ring current effects. In view of the general difficulty to predict ¹⁹F chemical shifts^{5,6}, other less well understood contributions were excluded from the calculations. Hence, the predictions only reflect the effects of ring current shifts related to relative changes in position and orientation of aromatic residues that are in close vicinity to ^{TET}C344^{7.54}. The positions of the predicted chemical shifts are shown superimposed as filled triangle shapes for the cyanopindolol bound β_1 AR (green) and for the full agonist isoprenaline bound and nanobody Nb80 coupled β_1 AR (black). The predicted position of the cyanopindolol bound receptor was normalized to the experimentally observed peak position of the cyanopindolol bound receptor. The distance between the predicted chemical shift positions for the two receptor states is -0.16 ppm and is indicated as a black line. The experimental position of P3 is indicated with a grey box. The latter peak is found to be exchanging with P2. (b) The crystal structure of the cyanopindolol bound β_1 AR (PDB ID 2YCY) is shown as blue cartoon. The position of ^{TET}C344^{7.54} is shown as magenta spheres. Aromatic residues predicted to influence the chemical

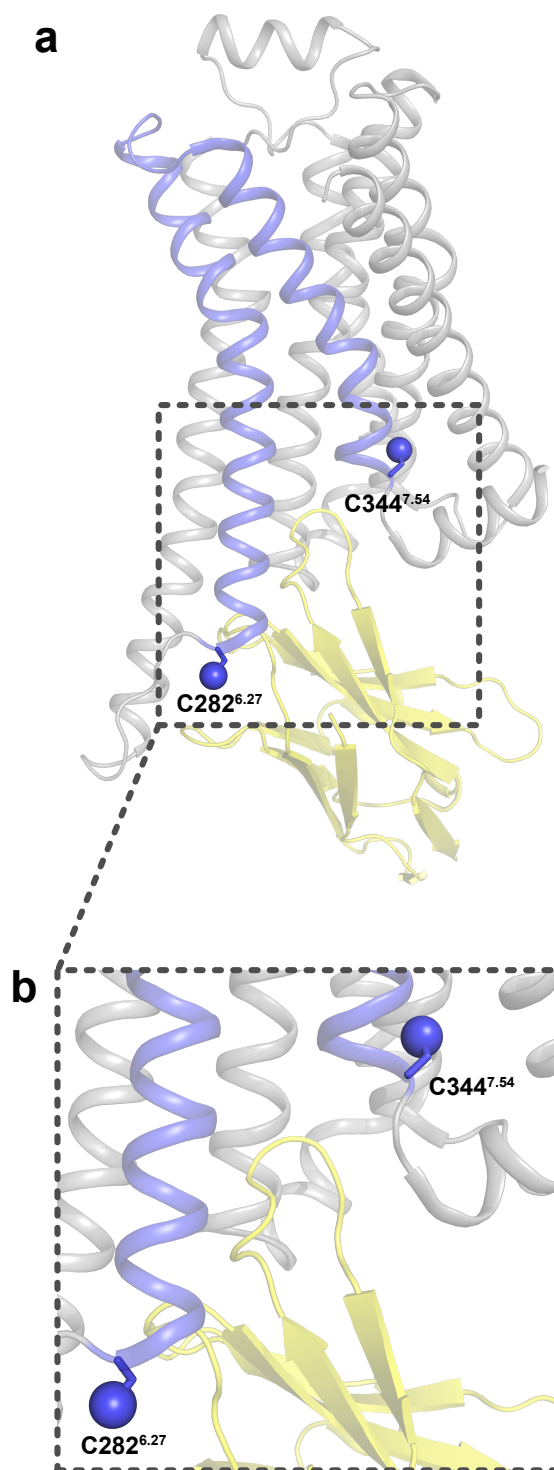
shift of $^{TET}C344^{7.54}$ are shown. In this case this is the neighbouring $Y343^{7.53}$ depicted in green. β_1AR has a very low basal activity which would make the apo state the most representative for the inactive state of β_1AR . However, in the absence of an available crystal structure of the apo state the cyanopindolol structure was used instead. Weak agonist bound crystal structures of thermostabilized β_1AR are all very similar in the cytoplasmic region of TM6 and TM7, where they are believed to show a conformation representative of an inactive state ⁷. **(c)** The crystal structure of the isoprenaline and nanobody Nb80 bound β_1AR (PDB ID 6H7J) is shown as pink cartoon. The position of $^{TET}C344^{7.54}$ is shown as magenta spheres. $Y343^{7.53}$ and $F349^{8.50}$ influence the predicted chemical shift of $^{TET}C344^{7.54}$ and are shown as green and cyan spheres, respectively. The orientation of the aromatic residues in the ternary state was assumed to be representative of their orientation in the pre-active state P3 (further details related to the calculations are provided in Supplementary Table 3).



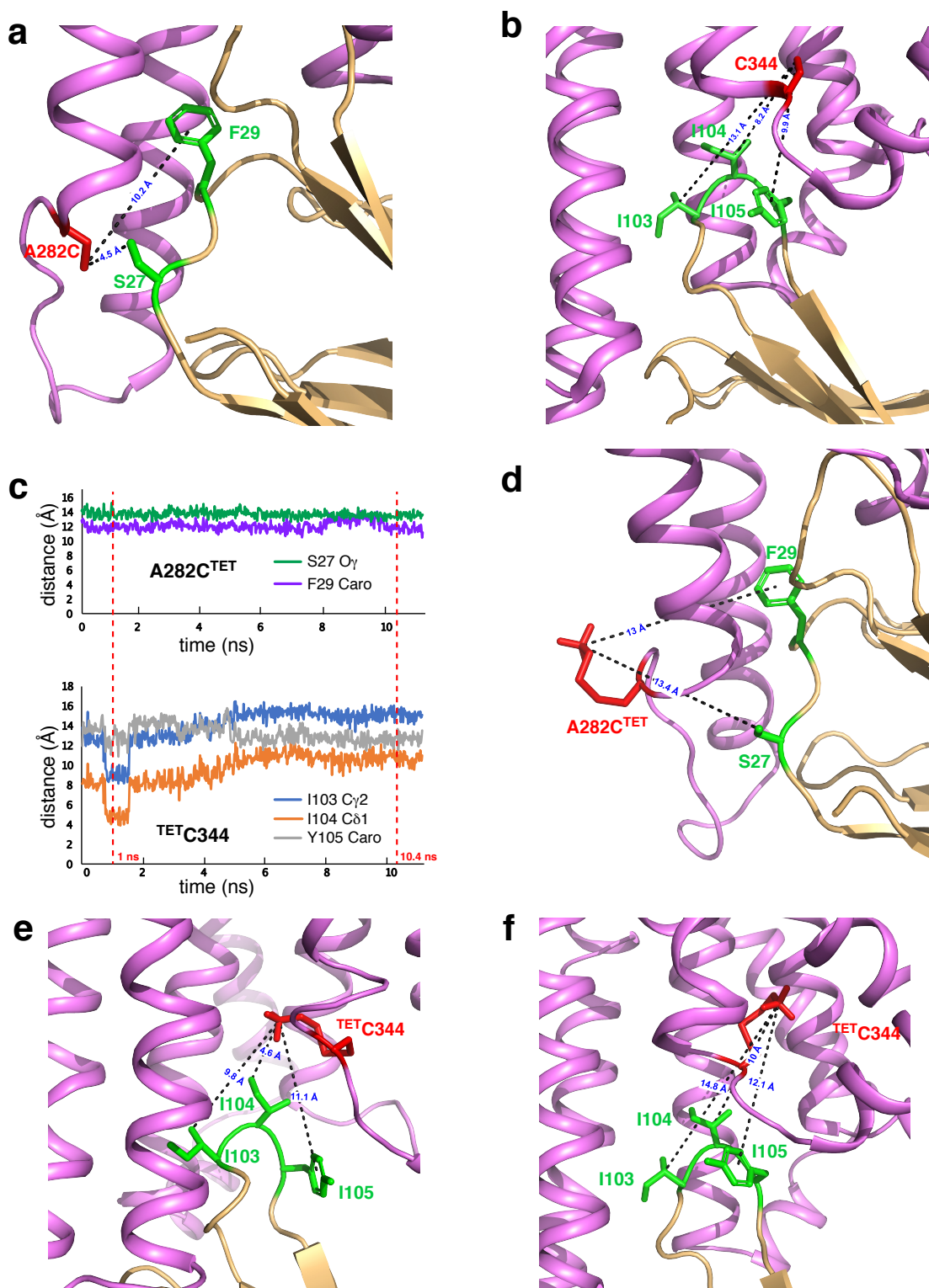
Supplementary Fig. 15 Overlay of active state crystal structures of β_1 AR ternary complexes bound to agonists of varying efficacies and G_s mimicking nanobodies. The crystal structures of ternary complexes with cyanopindolol (yellow, PDB code 6H7O), xamoterol (pink, PDB code 6H7N) and isoprenaline (cyan, PDB code 6H7J). Enlarged side-on view of the cytoplasmic region of β_1 AR TM7 and helix 8 with the residues of the conserved Np $xxY^{7.53}$ motif shown as sticks and the sulfur atom of the reporter C344^{7.54} shown as a sphere. The overlay reveals the structures as virtually identical. The nanobody was excluded from the overlay for clarity.



Supplementary Fig. 16 Comparing the location of aromatic residues in the vicinity of the TM7 reporter for β_1 AR and β_2 AR. The top panel shows the comparison of inactive (light yellow, PDB code 2YCY) and active (bright yellow, PDB code 6H7J) crystal structures of the β_1 AR. The bottom panel shows the inactive (dark pink, PDB code 4GBR) and active (light purple, PDB code 3SN6) structures of β_2 AR. The location of the TET probe is shown as red sphere attached to C344^{7.54} or C327^{7.54}, respectively. Proximal aromatic residues are displayed in blue. For both receptors, these residues correspond to the positions of Y^{7.53}, F^{8.50}, F^{8.54}. Both receptors show an inward rotation of TM7 upon activation which causes a change in the relative orientation of the C^{7.54} probe to the aromatic residues.

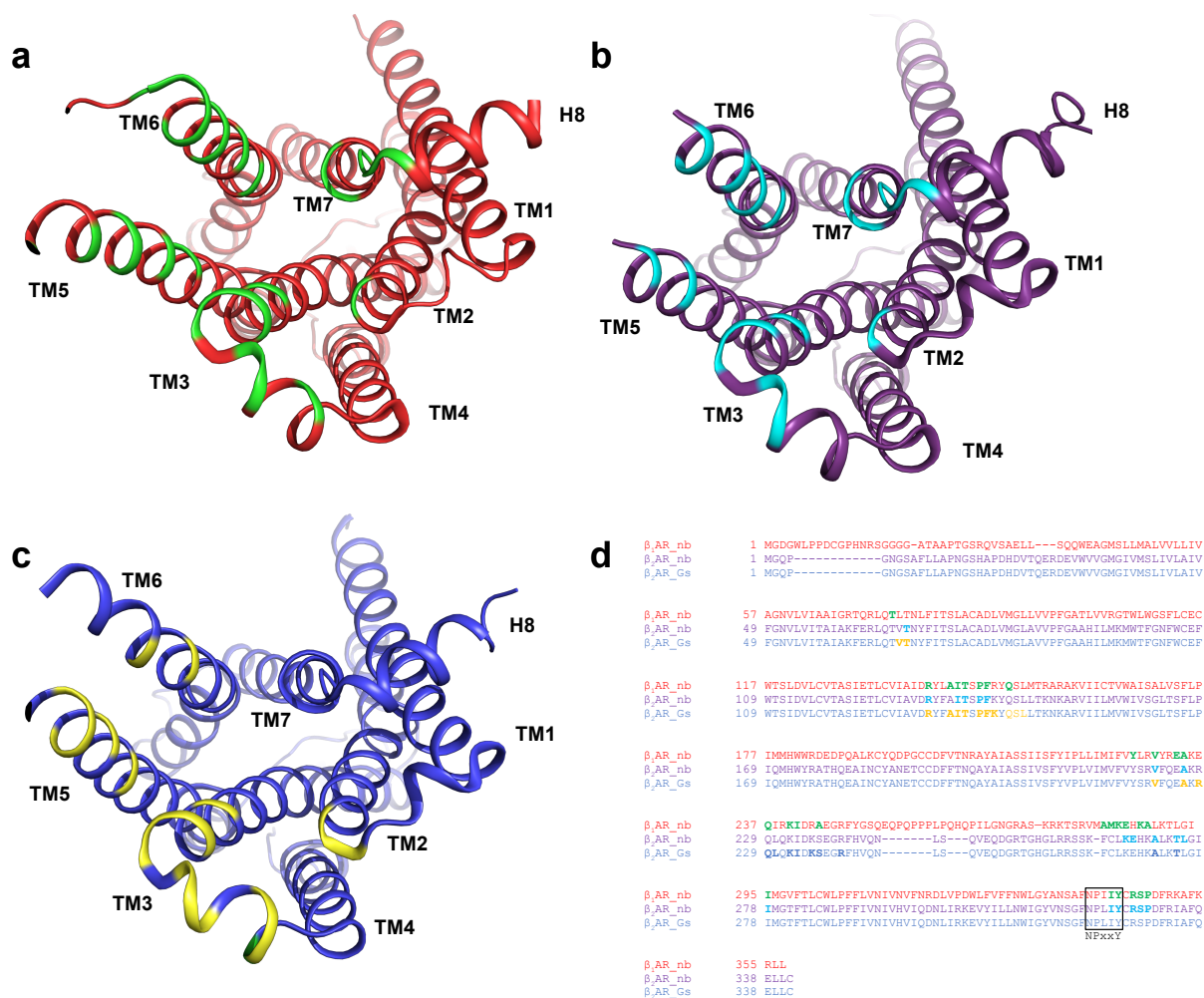


Supplementary Fig. 17 Ternary structure of the turkey β_1 AR bound to the partial agonist xamoterol and the nanobody Nb6B9 showing the receptor in a conformation corresponding to the fully active state (PDB ID 6H7N). (a) Side-on view of the ternary complex with β_1 AR shown in grey. TM6 and TM7 of the receptor are colored in blue with the TET labelling sites A282C^{6.27} and C344^{7.54} used in this study highlighted as blue spheres. The nanobody is colored in yellow. (b) Enlarged view of the cytoplasmic binding pocket.



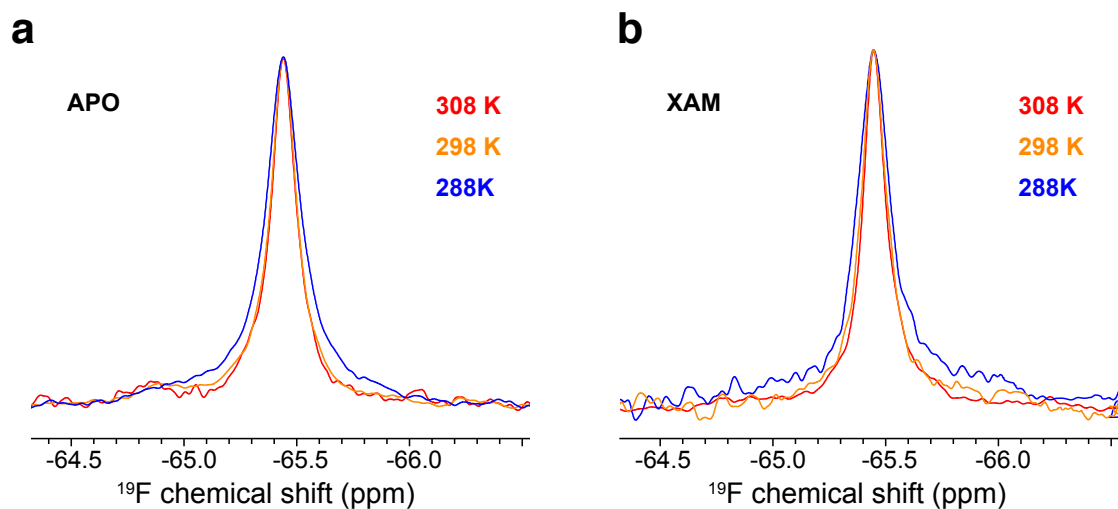
Supplementary Fig. 18 Nanobody residues in proximity to the ^{19}F NMR probes: receptor-nanobody binding interface in the ternary complex of xamoterol-bound turkey $\beta_1\text{AR}$ coupled to nanobody Nb6B9 (PDB ID 6H7N). (a,b,d,e,f) Cartoon representation of the cytoplasmic region of $\beta_1\text{AR}$ (pink) and the region of the nanobody (cream) interacting with the receptor. Nanobody residues in close proximity to the ^{19}F probe locations on TM6 and TM7 of $\beta_1\text{AR}$ are represented with their side chains as sticks (green). The ^{19}F probe locations are approximated by: (a) S_γ of TM6 A282C^{6,27} (red), (b) S_γ of TM7 C344^{7,54} (red), (d) CF_3 of

A282C^{TET,6.27} (red), and **(e, f)** CF₃ of ^{TET}C344^{7.54} (red). The shortest distances between nanobody and the ¹⁹F probes are highlighted by dashed black lines, with the distances indicated in blue. Distances given in (a) and (c) are based on the unmodified coordinates of the crystal structure and correspond to a situation where the location of the ¹⁹F probe is approximated by the S_γ position. Aiming to obtain better representative positions for the fluoro probes, TET tags were added to the S_γ positions resulting in A282C^{TET} and ^{TET}C344. The conformational energy of the structure with the tagged cysteines was subsequently minimized and a MD simulation conducted with the receptor embedded in a fully hydrated POPC bilayer. **(c)** MD trajectories showing the shortest distances between nanobody residues S27 (O_γ) or F29 (Caro) and the CF₃ of A282C^{TET} **(c, upper)**, and between the nanobody residues I103 (C_{γ2}), I104 (C_{δ1}) or Y105 (Caro) and the CF₃ of ^{TET}C344 **(c, lower)** as a function of the simulation time. For A282C^{TET} the distances remain very similar during the entire simulation. For ^{TET}C344, however, the simulation reveals two side chain orientations. A minor conformer at ca. 1 ns that exists for ca 8% of the simulation and shows shorter distances to the nanobody, while for the remainder of the simulation (92%) the distances are considerably larger. **(e)** Snapshot taken at 1 ns representative of the minor conformer (c, red dashed line) with the orientation of ^{TET}C344 pointing in direction of TM6 that results in reduced distances to the nanobody. **(f)** Snapshot taken at 10.4 ns (c, red dashed line) representative of the major conformer where the distances from the CF₃ of ^{TET}C344 to the nanobody are substantially increased.

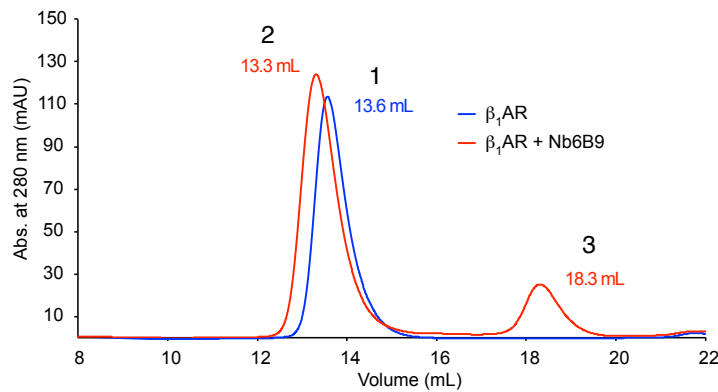
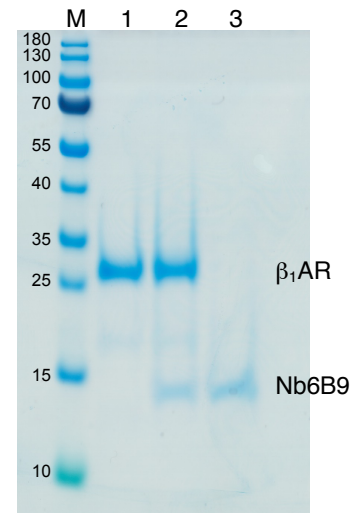


Supplementary Fig. 19 Binding interface receptor residues in ternary complex between

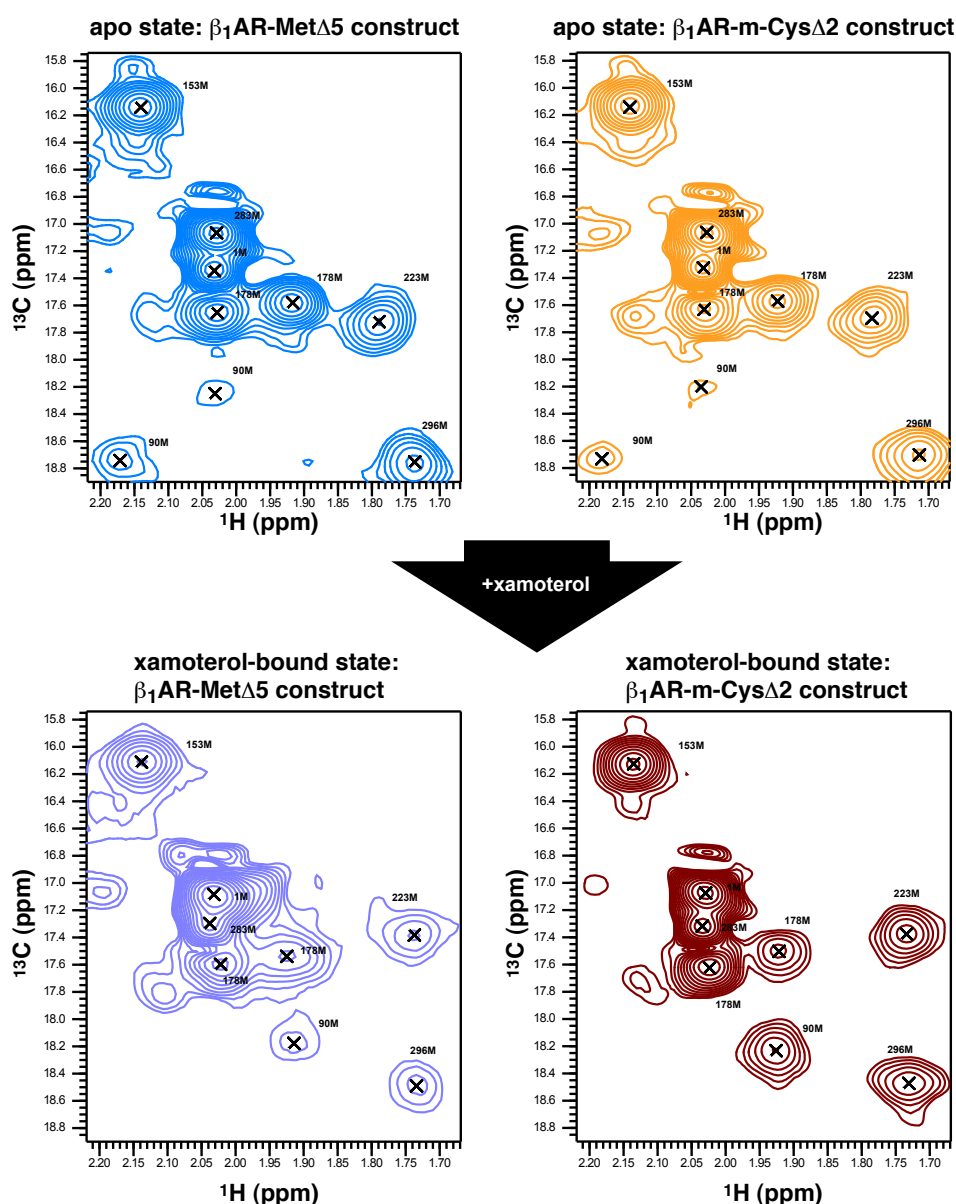
β_1AR or β_2AR and intracellular binding partners (IBPs). Cytoplasmic view of β_1AR and β_2AR in ternary complex, with the residues with atoms within 3.8 Å of the binding partner highlighted. The IBPs are omitted from the figure for clarity. **(a)** The β_1AR (PDB code 6H7J) is shown as a red cartoon and residues in contact with the nanobody Nb80 are highlighted in green. The positions of the individual helices are indicated. **(b)** The β_2AR (PDB code 3P0G) is shown as purple cartoon and residues in contact with the nanobody Nb80 are highlighted in cyan. **(c)** The β_2AR (PDB code 3SN6) is shown as blue cartoon and residues in contact with the G_α subunit of the heterotrimeric G_s protein are highlighted in yellow. **(d)** Sequence alignment of the receptors shown in (a) to (c) with the IBP interacting receptor residues highlighted using the same colour scheme. The NPxxY⁷⁻⁵³ motif on TM7 is indicated by a box. While no TM7 interactions are observed in the G_s structure of β_2AR , interactions involving the TM7 region leading into H8 are similar for β_1AR and β_2AR bound to nanobodies, with five residues in the TM7-helix 8 region being part of the binding interface.



Supplementary Fig. 20 Temperature dependent ¹⁹F NMR spectra of β_1 AR TM7^{TET}C344^{7.54} in the apo form and bound to xamoterol. Overlay of spectra showing the signal P2 recorded at the temperatures of 308 K (red), 298 K (orange) and 288 K (blue) for the receptor in the apo form (**a**) and bound to xamoterol (**b**). Over the temperature range investigated there is no evidence of multiple signal components for the P2 signal.

a**b****Supplementary Fig. 21 β_1 AR ternary complex formation demonstrated by SEC and SDS-**

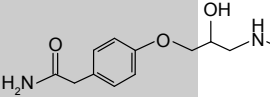
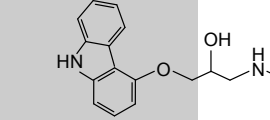
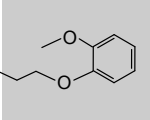
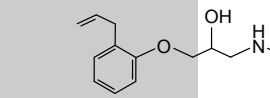
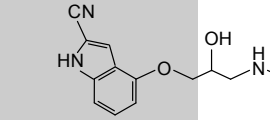
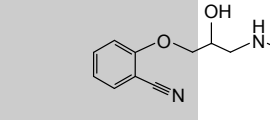
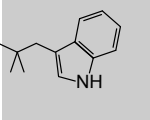
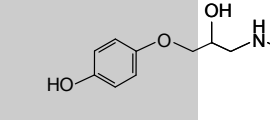
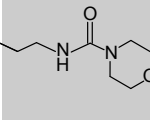
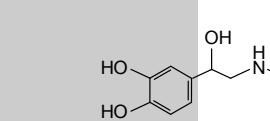
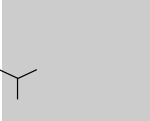
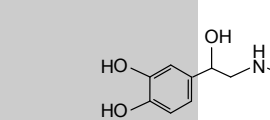
PAGE analysis. 14 μ M β_1 AR-m-Cys Δ C2 solubilized in LMNG were incubated with 1 mM isoprenaline and 21 μ M Nb6B9. **(a)** SEC (Superdex S200 10/300) traces of isoprenaline-bound β_1 AR-m-Cys Δ C2 in the absence (blue), and in the presence of nanobody Nb6B9 (red), showing formation of the ternary receptor complex (peak 2). **(b)** SDS-PAGE analysis of the SEC fractions. SEC fraction peak numbers and SDS-page lane numbers correspond to each other. M, molecular weight marker; lane 1, β_1 AR; lane 2, ternary complex of isoprenaline-bound β_1 AR-m-Cys Δ C2 complexed with Nb6B9 nanobody; lane 3, unbound nanobody.



Supplementary Fig. 22 Receptor functionality of β_1 AR-Cys Δ 2 demonstrated by ^{13}C methyl methionine NMR. Comparison of ^1H , ^{13}C HMQC spectra of ^{13}C -Met β_1 AR-Met Δ 5 (used in the study by Solt et al 2017 (ref ¹⁷ in main text) and ^{13}C -Met β_1 AR-m-Cys Δ 2 with $^{\text{TET}}\text{C344}^{7,54}$ (used in this study) in the apo form and bound to xamoterol. Both receptors show equal spectral appearance in the apo form and the same behaviour upon activation through binding of the partial agonist xamoterol. It is concluded that the two receptor constructs behave very similarly and that the presence of the Cys Δ 2 mutation and TET tagging at C344 has no deleterious effect on the functional response of the receptor construct β_1 AR-m-Cys Δ 2. Experiments were recorded at 800 MHz (^1H) and 308 K.

Supplementary Table 1

Pharmacological properties of agonists used in this study

| Ligand name | Log K _D [#] | G _S efficacy [§] (% isoprenaline) | Chemical structure | |
|---------------|---------------------------------|--|--|---|
| | | | Head | Tail |
| atenolol | -5.40 ± 0.06 | 2.1 |  |  |
| carvedilol | -9.43 ± 0.05 | 12 |  |  |
| alprenolol | -7.96 ± 0.04 | 31 |  |  |
| cyanopindolol | -10.89 ± 0.06 | 34 |  |  |
| bucindolol | -9.43 ± 0.06 | 49 |  |  |
| xamoterol | -6.58 ± 0.02 | 67 |  |  |
| isoprenaline | -6.86 ± 0.08 | 100 |  |  |
| adrenaline | -6.01 ± 0.04 | 108 |  |  |

[#]Data taken from Baker et al. 2010 ⁸

[§]Data taken from Baker et al. 2011 ⁹

Supplementary Table 2

¹⁹F chemical shift positions and R_2 values of β_1 AR TM6 A282C^{TET} and TM7^{TET}C344, for ligand-bound receptor and for receptor in ternary complex coupled to Nb6B9 (chemical shift positions and R_2 values were obtained from signal deconvolutions using Lorentzian lines)

| Ligand | Abbr. | Efficacy | peak [#] state [†] Nb6B9 [‡] | TM6 A282C ^{TET} | | | | | TM7 ^{TET} C344 | | | | | | | |
|---------------|-------|----------|---|---------------------------------------|-----------------|-------------------------|-----------------|--------------------|---------------------------------------|-----------------|------------------|-----------------|-------------------------|-----------------|------------------|-----------------|
| | | | | Chemical shifts [§] (ppm) | | R_2 (Hz) [§] | | | Chemical shifts [§] (ppm) | | | | R_2 (Hz) [§] | | | |
| | | | | P1 | P4 | P1 | P4 | P1/P7 [‡] | P2 | P5 | P2 [§] | P6 [§] | P2 | P5 | P2 [§] | P6 [§] |
| | | | | I ₁ | A ^{G+} | I ₁ | A ^{G+} | I/A ^{G-} | I _{1,2} | A ^{G+} | I _{1,2} | A ^{G-} | I _{1,2} | A ^{G+} | I _{1,2} | A ^{G-} |
| | | | no | yes | no | yes | yes | no | yes | yes | yes | no | yes | yes | yes | |
| ligand free | APO | | 2x | -66.33 | -65.44 | 115 | 75 | 130 | -65.42 | -64.69 | -65.42 | -65.42 | 80 | 320 | 75 | 300 |
| atenolol | ATE | 2 | - | -66.37 | | 115 | | | -65.43 | | | | | | | |
| carvedilol | CVD | 12 | 2x | -66.34 | -65.45 | 118 | 75 | 120 | -65.43 | -64.57 | -65.43 | -65.55 | 80 | 250 | 82 | 250 |
| alprenolol | ALP | 31 | - | -66.33 | | 120 | | | -65.41 | | | | | | | |
| cyanopindolol | CYA | 34 | 2x | -66.37 | -65.47 | 122 | 95 | 120 | -65.42 | -64.71 | -65.47 | -65.55 | 80 | 230 | 80 | 330 |
| Bucindolol | BUC | 49 | 2x | | | | | | -65.47 | -64.68 | -65.47 | -65.50 | | | | |
| xamoterol | XAM | 67 | 2x | -66.35 | -65.44 | 130 | 92 | 170 | -65.46 | -64.78 | -65.45 | -65.51 | 100 | 270 | 103 | 240 |
| xamoterol | XAM | 67 | 5x | | | | | | -65.46 | -64.77 | -65.46 | -65.52 | 100 | 270 | 105 | 250 |
| xamoterol | XAM | 67 | 10x | | | | | | -65.46 | -64.78 | -65.45 | -65.52 | 100 | 260 | 100 | 260 |
| isoprenaline | ISO | 100 | 2x | -66.31 | -65.45 | 140 | 106 | | -65.47 | -64.77 | | (-65.42) | 140 | 320 | | (200) |
| adrenaline | ADR | 108 | - | | | | | | -65.47 | | | | 160 | | | |

[#]Peak numbering as discussed in the main text and shown on the spectra

[†]Receptor states as discussed in the main text

[§]Chemical shift positions and R_2 values were obtained from deconvolution with Lorentzian lines

[§]For TM7 in the presence of nanobody the overlapped high field region containing P2 and P6 signals was deconvoluted with two Lorentzian lines (Supplementary Fig. 8) resulting in significantly improved fits for this region, as evidenced by the smaller residuals. For the isoprenaline complex the signal-to-noise of the P2/P6 region was too low to justify deconvolution using two Lorentzians lines. Instead, deconvolution of the P2/P6 region was conducted using a single Lorentzian line thus resulting in an R_2 value between the ones for the P2 and P6 signals.

[‡]The existence of P7 on TM6 is based on the observations for the corresponding peak P6 on TM7, which infers the presence of the (A^{G-}) form also for TM6. The chemical shift of P7 is almost identical to P1 and the presence of P7 therefore only shows via changes in linewidth as the amount of nanobody is varied. The existence of P7 is not discussed in the main text, but its presence mirrors the behaviour of P6 on TM7.

[‡]The factors (2x, 5x, 10x) relate to the excess of Nb6B9 over β_1 AR. 'no' means: in the absence of Nb6B9; 'yes' means: in the presence of Nb6B9

Supplementary Table 3

Predicted and observed ^{19}F chemical shift positions for $\beta_1\text{AR}$ TM6 A282C and TM7 C344, for ligand-bound receptor and for receptor in ternary complex coupled to nanobody

| State | Mutation | TM6 A282C | | | | | TM7 C344 | | | | |
|-------------------------|----------|------------------------|-------------------------------------|-----------------------------|--|------------------------------------|------------------------|-------------------------------------|---|--|------------------------------------|
| | | Ring-current shifts | | Experimental | | | Ring-current shifts | | Experimental | | |
| | | Predicted [§] | $\Delta\delta(\text{CYA})^\ddagger$ | Observed | $\Delta\delta(\text{CYA}, \text{P1})^\ddagger$ | Contributions > 10.01 [¶] | Predicted [§] | $\Delta\delta(\text{CYA})^\ddagger$ | Observed | $\Delta\delta(\text{CYA}, \text{P2})^\ddagger$ | Contributions > 10.05 [¶] |
| CYA [#] | L282C | -0.028 | 0 | P1: -66.37 | P1: 0 | Tyr 149 Tyr 231 | 0.024 | 0 | P2: -65.42 | P2: 0 | Tyr 343 |
| ISO + Nb80 [§] | A282C | -0.003 | 0.025 | +Nb6B9 P4: -65.45 | P4: +0.92 | - | -0.133 | -0.157 | +Nb6B9 P5: -64.77 P3: -65.95 | P5: +0.65 P3: -0.53 | Tyr 343 Phe 349 |

[#]Predictions using PDB structure 2YCY, chain A

[§]Predictions using PDB structure 6H7J, chains A & C

^{*}In order to predict the ring current shift for C282, crystal structures were mutated to cysteine using the mutagenesis function in Pymol ¹⁰, with the backbone-dependent rotamer giving minimum steric clashes selected

[¶]Residues contributing >10.01 and > 10.05 ppm to the predicted ring-current shift for C282 and C344 respectively.

[§]Ring-current chemical shifts for cysteine H γ were calculated based on the Johnson-Bovey equation ⁴ as implemented in MolMol ³ using the crystallographic coordinates. Protons were added using UCSF Chimera ¹¹. Calculations used the preferred crystallographic chain as reported in the GPCRdB ¹².

[‡]Chemical shift difference calculated relative to the cyanopindolol-bound form. For experimentally observed shifts, the inactive state signal, P1 or P2 for C282 and C344 respectively, is used.

Supplementary Table 4**Primer sequences used for site-directed cysteine mutagenesis**

| | | |
|--------------|---------|---------------------------|
| C85V | Forward | GTGGCCGACCTGGTGAT |
| | Reverse | GGCCAGCGAGGTGATGAAG |
| C163L | Forward | CTGACCGTCTGGGCCATCTCC |
| | Reverse | GATGATGACCTTGGCCCGAGC |
| C344S | Forward | ATCATCTACTCCCGCAGCCC |
| | Reverse | GGGGTTGGCAGCAGAGTT |
| A282C | Forward | TGTCGCCTGCATGAGGGAACACAAA |
| | Reverse | CGGGACGTCTTCCTCTTGCTA |

Supplementary Note 1: β_1 AR constructs and ^{19}F labelling of cysteines

Previously we studied the activation of the β_1 AR using ^{13}C methyl-methionine NMR spectroscopy, focusing on the TM region of the receptor¹³. To relate this ^{19}F NMR study to our previous investigation, we set out from the same β_1 AR-Met Δ 5 construct¹³, named β_1 AR-m, that relative to wild type contains three thermostabilising mutations, with the number of methionine residues reduced by five (Supplementary Fig. 1) (see Methods). The functionality of the construct was shown previously¹³. Of the six reduced cysteines available in β_1 AR-m, native C344^{7.54} was suitable for fluoro-tagging to report on the cytoplasmic region of TM7 during receptor activation (Supplementary Fig. 1a). A separate reporter cysteine at the end of TM6 was introduced in a second construct as A282C^{6.27}, while removing the TM7 cysteine via a C344S^{7.54} mutation, resulting in β_1 AR-m-TM6 (Supplementary Fig. 1b). To permit a direct comparison with our previous ^{13}C NMR study all experiments were conducted with receptor solubilized in LMNG micelles.

Tests using 3-bromo-1,1,1-trifluoroacetone (BTFA) resulted in the labelling of multiple cysteine sites and were abandoned, despite the use of constructs where two accessible Cys residues on TM2 and TM4 were replaced as C85V^{2.48} and C163L^{4.47}, leading to β_1 AR-m-Cys Δ 2 (Supplementary Fig. 1a) and β_1 AR-m-TM6-Cys Δ 2 (Supplementary Fig. 1b). Further attempts with 2-bromo-N-[4-(trifluoromethyl)phenyl]acetamide (BTFMA) resulted in receptor that was unable to bind nanobody Nb6B9 (Supplementary Fig. 3). Labelling with 2,2,2-trifluoroethanethiol (TET) following the described two step reaction (Supplementary Fig. 2)¹, resulted in the required selective ^{19}F tagging of β_1 AR-m-Cys Δ 2 at $^{\text{TET}}\text{C344}^{7.54}$ and β_1 AR-m-TM6-Cys Δ 2 at A282C $^{\text{TET},6.27}$ (Supplementary Fig. 4a). ^{19}F labelled Cys Δ 2 receptor constructs showed identical responses towards ligand and nanobody binding as the β_1 AR-m based receptor constructs, but the presence of C85^{2.48} and C163^{4.47} in the latter produced unstable receptor due to tagging at multiple internal sites, which substantially reduced the yield of receptor labelled exclusively at A282C^{6.27} or C344^{7.54}, respectively (Supplementary Fig. 5). Hence, all NMR studies were conducted using the two Cys Δ 2 constructs of β_1 AR. The ^{19}F labelled NMR samples were purified to homogeneity (Supplementary Fig. 4b) and ^{19}F NMR assignments were obtained based on the unique complementarity of the non-overlapping A282C $^{\text{TET},6.27}$ and $^{\text{TET}}\text{C344}^{7.54}$ signals (Supplementary Fig. 4a). While all of the receptors were stable over several days at 308 K the slow cleavage of the S-S bond resulted in the gradual release of small amounts of free TET over time, which became visible in the NMR spectra. This however does not interfere with any of our investigations.

Supplementary Note 2: Solvent accessibility of the TM7 ^{TET}C344 environment

The response of the TM7 ^{TET}C344^{7.54} environment upon addition of a water-soluble Gd³⁺ paramagnetic relaxation reagent was investigated for xamoterol-bound β_1 AR-m-Cys Δ 2 in the presence of a two-fold excess of nanobody through titration with increasing amounts (0 - 5 mM) of gadopentetic dimeglumine (Magnevist). The reaction conditions permitted a side-by-side comparison of the ligand-bound receptor via the P2 signal and the ternary receptor via the P5 signal. Signal intensity losses for P5 related to Gd³⁺ addition were more pronounced than for P2 and increases in R_2 values (determined from a two-point measurement) for P5 were more substantial than for P2 (Supplementary Fig. 11). Relaxation enhancements $\varepsilon = 32.87 \text{ s}^{-1}\text{mM}^{-1}$ for P5 and $\varepsilon = 8.29 \text{ s}^{-1}\text{mM}^{-1}$ for P2 were obtained from the slopes of the linear fits to the R_2 rates. The measurement series established the ternary ^{TET}C344^{7.54} receptor environment relating to the P5 signal to be significantly more solvent-accessible than in the ligand-bound receptor as assessed by the P2 signal.

Supplementary Note 3: Response of TM6 A282C^{TET, 6.27} to agonist binding

The P1 signal for A282C^{TET, 6.27} showed only a relatively small response to ligand binding upon probing the receptor with a range of agonists varying in efficacy (Fig. 2a, Supplementary Fig. 6a). A small amount of exchange broadening to R_2 became apparent when comparing the apo receptor with isoprenaline bound β_1 AR, indicating the presence of smaller amounts of μs -to- ms conformational dynamics when bound to higher efficacy ligands (Supplementary Table 2). Compared to our previous methionine ¹³C NMR study, this relatively small effect initially appeared counterintuitive, as β_1 AR-m showed strong responses in ¹H and ¹³C to agonist activation as evidenced by a range of reporters, including those on TM4, TM5 and TM6 (M153^{4.37}, M178^{4.62}, M223^{5.54} and M296^{6.41})¹³. Also, as shown by Liu et al. for β_2 AR, the equivalent position, ^{TET}C265^{6.27}, on TM6 was observed in a slow-exchanging equilibrium between two states postulated as inactive and active receptor forms, that changed their populations in an agonist-efficacy dependent manner; in contrast to our observations with P1². It has been shown that aromatic residues in the proximity of a fluoro probe can have a considerable effect on the position of the observed ¹⁹F NMR signal via ring current shifts¹⁴. Inspection of the molecular environment of A282C^{6.27} in β_1 AR showed a complete lack of aromatic residues in its vicinity, in contrast to the equivalent region in β_2 AR (Supplementary Fig. 12) or to M296^{6.41} in β_1 AR¹³. Using the β_1 AR crystal coordinates of several ligand-bound structures we calculated the expected ring current shifts for A282C^{TET} for different states compared to the inactive state (PDB code 2YCY) (Supplementary Fig. 13, Supplementary Table 3). In all cases, these calculated shift changes were smaller than 0.05

ppm, even when considering β_1 AR active receptor states in ternary complex with nanobody, emphasizing that due to the local environment lacking aromatic residues and A282C^{6,27} pointing towards the solvent, in the absence of changes in solvent accessibility the fluoro probe is unable to report on conformational changes at this position. Unsurprisingly therefore, the TM6 signal showed relatively minor changes upon ligand binding to the receptor (Supplementary Fig. 6a). It can be assumed therefore that the small amount of additional broadening observed in the isoprenaline bound form is related to exchange between conformations that differ only little in their chemical environments. Little chemical shift response in this region was also observed in the study by Isogai et al. for the backbone amide environment of V280^{6,25}, consistent with our data¹⁵. As evidenced in our study by the increase in R_2 values for P1 from the apo receptor to the isoprenaline bound form (Supplementary Table 2), it can be assumed that despite the lack of chemical shift perturbations, conformational interchange on TM6 is taking place. However, the similarity in chemical shifts between exchanging states when compared to β_2 AR places this process in β_1 AR on the fast-to-intermediate timescale, with relatively minor impact on the observed linewidth of P1.

Supplementary Note 4: Increased solvent accessibility of the TM7^{TET}C344 environment in the ternary complex

Titration with the paramagnetic relaxation reagent Magnevist established the cytoplasmic TM7 environment of the ternary complex to be more solvent accessible than in the ligand bound states. For TM7 C344^{7,54} this supports the proposition where the observed downfield shift of P5 (compared to P2, P3) is caused by a greater solvent exposure in the ternary complex as the ¹⁹F probe relocates from the more hydrophobic environment sampled in the ligand-bound states (Fig. 5). Based on this accessibility data obtained with xamoterol as ligand it seems reasonable to suggest that the comparable chemical shift changes observed upon formation of the ternary complexes with the other agonists relate to similar effects. Further, as the size of the chemical shift changes between ligand-bound receptor and ternary complexes for TM6 and TM7 are of similar size we suggest that a similar explanation holds also for the changes observed for A282C^{TET, 6,27} on TM6. Other potential sources contributing towards the observed chemical shift changes need to be considered, such as the proximity of nanobody residues in or near the binding interface in the ternary complexes (Supplementary Fig. 17). We assessed the likely contribution of such effects by measuring the distances of nanobody residue side chains to the S γ positions of A282C and C344, respectively, using the crystal structure of β_1 AR in the ternary state in complex with xamoterol and Nb6B9 (PDB ID 6H7N) (Supplementary Fig. 18a,b). However, the S γ locations only provide an approximate estimate of the ¹⁹F probe positions. To obtain more representative distances we added the TET moieties onto the aforementioned cysteine residues and conducted a 12 ns MD

simulation of the ternary complex equilibrated in a fully hydrated POPC lipid bilayer (Supplementary Fig. 18c). While the simple analysis using distances to S_{γ} suggested S27 as a residue close to A282C (4.5 Å) (Supplementary Fig. 18a), the simulation showed no proximal residues within 13 Å of the A282C^{TET} CF₃ group (Supplementary Fig. 18d). For C344 all distances to S_{γ} were relatively large, with I104 closest at 8.2 Å (Supplementary Fig. 18b). The simulation revealed a minor conformer with a population of only 8% with a short distance from the CF₃ of ^{TET}C344 to I104 C δ 1 (4.6 Å) (Supplementary Fig. 18e), while in contrast for the remaining time of the simulation (92% population) all distances in the sampled conformers were beyond 8 Å (Supplementary Fig. 18f).

Based on these distances we did not find any conclusive evidence for nanobody residue proximity related effects as a substantial contribution towards the observed changes in ¹⁹F chemical shifts. Overall, the increased solvent-accessibility for TM6 A282C and TM7 C344 following a move into a less hydrophobic environment seems to provide the most consistent explanation for the prominent downfield shifts observed upon ternary complex formation, as proposed above.

Supplementary Note 5: Interactions between β_1 AR and Nb6B9 in the ternary complex

A caveat needs to be added regarding the usage of nanobodies such as Nb6B9 as their primary purpose resides in stabilizing a GPCR in a native-like fully active state, while they are a poor mimetic of extended G_{α_s} function. The similarity of nanobody as well as G_s bound structures of β_2 AR in the TM7-helix 8 region is very high. However, in the crystal structure of β_2 AR in the full G_s protein complex TM7 lacks direct interactions with the heterotrimeric G_s protein, while both β_2 AR and β_1 AR in nanobody complexes show five residues in the TM7-helix 8 region that form contacts, including the last two residues of the NPxxY^{7.53} motif (Supplementary Fig. 19)¹⁶. Crystallography shows several ternary Nb6B9 and Nb80 complexes of β_1 AR bound to a range of agonists of varying efficacy with TM7 conformations near the NPxxY motif that are nearly identical (Supplementary Fig. 15). This is in clear contrast to our NMR work in solution. Possibly the differences are the result of crystal packing effects making the static structure information in this area of the receptor unreliable.

Supplementary Methods: BTFA/BTFMA ¹⁹F labelling protocol

Purified β_1 AR receptor eluted from an NiNTA purification was collected and the solution adjusted to 10 μ M in protein via concentration (Amicon Ultra-15 spin concentrator with 50 kDa molecular weight cutoff). The labelling reagent 3-bromo-1,1,1-trifluoroacetone (BTFA) or 2-bromo-N-(4-(trifluoromethyl)phenyl)acetamide (BTFMA), respectively, was added in a tenfold molar excess to a cold solution of the receptor and stirred gently for 1 h at 4 °C. The labelling reaction was terminated through removal of the labelling reagent through dilution concentration (1000x) or desalting using a HiTrap desalting column (GE Healthcare) into buffer containing 50 mM Tris pH 8, 350 mM NaCl and 0.02% (w/v) LMNG. The labelled receptor was further purified by alprenolol ligand affinity chromatography and eluted with either 1 mM atenolol or 0.1 mM alprenolol.

Supplementary References

1. Klein-Seetharaman, J., Getmanova, E. V., Loewen, M. C., Reeves, P. J. & Khorana, H. G. NMR spectroscopy in studies of light-induced structural changes in mammalian rhodopsin: applicability of solution (19)F NMR. *Proc. Natl. Acad. Sci. U. S. A.* **96**, 13744–13749 (1999).
2. Liu, J. J., Horst, R., Katritch, V., Stevens, R. C. & Wüthrich, K. Biased signaling pathways in β_2 -adrenergic receptor characterised by ^{19}F -NMR. *Science* **335**, 1106–1110 (2012).
3. Koradi, R., Billeter, M. & Wüthrich, K. MOLMOL: A program for display and analysis of macromolecular structures. *J. Mol. Graph.* **14**, 51–55 (1996).
4. Johnson, C. E. & Bovey, F. A. Calculation of nuclear magnetic resonance spectra of aromatic hydrocarbons. *J. Chem. Phys.* **29**, 1012–1014 (1958).
5. Kitevski-LeBlanc, J. L. & Prosser, R. S. Current applications of ^{19}F NMR to studies of protein structure and dynamics. *Prog. Nucl. Magn. Reson. Spectrosc.* **62**, 1–33 (2012).
6. Ye, L. *et al.* Mechanistic insights into allosteric regulation of the A_{2A} adenosine G protein-coupled receptor by physiological cations. *Nat. Commun.* **9**, 1372 (2018).
7. Warne, T. *et al.* Structure of a β_1 -adrenergic G-protein-coupled receptor. *Nature* **454**, 486–491 (2008).
8. Baker, J. G. A full pharmacological analysis of the three Turkey β -adrenoceptors and comparison with the human β -adrenoceptors. *PLoS One* **5**, (2010).
9. Baker, J. G., Proudman, R. G. W. & Tate, C. G. The pharmacological effects of the thermostabilising (m23) mutations and intra and extracellular (β 36) deletions essential for crystallisation of the turkey β -adrenoceptor. *Naunyn. Schmiedeberg's. Arch. Pharmacol.* **384**, 71–91 (2011).
10. The PyMOL Molecular Graphics System Version 2.0.
11. Pettersen, E. F. *et al.* UCSF Chimera - A visualization system for exploratory research and analysis. *J. Comput. Chem.* **25**, 1605–1612 (2004).
12. Pándy-Szekeres, G. *et al.* GPCRdb in 2018: adding GPCR structure models and ligands. *Nucleic Acids Res.* **46**, D440–D446 (2018).
13. Solt, A. S. *et al.* Insight into partial agonism by observing multiple equilibria for ligand-bound and Gs-mimetic nanobody-bound β_1 -Adrenergic receptor. *Nat. Commun.* **8**, 1–12 (2017).
14. Liu, D. & Wüthrich, K. Ring current shifts in ^{19}F -NMR of membrane proteins. *J. Biomol. NMR* (2016). doi:10.1007/s10858-016-0022-4
15. Isogai, S. *et al.* Backbone NMR reveals allosteric signal transduction networks in the β_1 -adrenergic receptor. *Nature* **530**, 237–241 (2016).
16. García-Nafria, J. & Tate, C. G. Cryo-EM structures of GPCRs coupled to Gs, Gi and Go. *Mol. Cell. Endocrinol.* **488**, 1–13 (2019).